AD_____

Award Number:
W81XWH-10-1-0766

TITLE:
A Computational Model of the Eye for Primary and Secondary Blast Injury

PRINCIPAL INVESTIGATOR:
Thao D. Nguyen, Kaliat T. Ramesh, Oliver Schein

CONTRACTING ORGANIZATION:

Johns Hopkins University
Baltimore, MD 21218

Á
REPORT DATE:
October 2012

Á
TYPE OF REPORT:
Annual

Á
PREPARED FOR: U.S. Army Medical Research and Materiel Command
                            Fort Detrick, Maryland 21702-5012

REPORT DOCUMENTATION PAGE

1. REPORT DATE (DD-MM-YYYY)	2. REPORT TYPE	3. DATES COVERED (From - To)
October 20	Annual	09/28/2011-10/27/2012

4. TITLE AND SUBTITLE	5a. Contract Number
A Computational Model of the Eye for Primary and Secondary Blast Injury	
	5b. GRANT NUMBER
	W81XWH-10-1-07
.	**5c. PROGRAM ELEMENT NUMBER**

6. AUTHOR(S)	5d. PROJECT NUMBER
Thao D. Nguyen, Rajneesh Bhardwaj	
	5e. TASK NUMBER
email: vicky.nguyen@jhu.edu	**5f. WORK UNIT NUMBER**

7. PERFORMING ORGANIZATION NAME(S) AND ADDRESS(ES)	8. PERFORMING ORGANIZATION REPORT NUMBER
Johns Hopkins University Baltimore, MD 21218	

9. SPONSORING / MONITORING AGENCY NAME(S) AND ADDRESS(ES)	10. SPONSOR/MONITOR'S ACRONYM(S)
US Army Medical Research and Materiel Command Fort Detrick, Maryland 21702-5012	
	11. SPONSOR/MONITOR'S REPORT NUMBER(S)

12. DISTRIBUTION / AVAILABILITY STATEMENT
Approved for public release; distribution unlimited

13. SUPPLEMENTARY NOTES

14. ABSTRACT
This report describes the FY12 research accomplishments and their significance. In this second year of the project, we focused on developing a computational model to assess the effects of facial features and deformability of ocular tissues on the blast impact. In addition, we have made significant progress towards developing a constitutive model for the stress response of the cornea and sclera that includes the anisotropic effects of the collagen fiber structure. Moreover, we have begun developing analysis methods for the dynamical inflation experiments. These accomplishments are important steps in examining all three hypotheses. We have made significant progress towards all three Specific Aims guiding the project

15. SUBJECT TERMS
dynamic inflation, shock tube system, digital image correlation, microstructure-based constitutive model, cornea, sclera, anisotropy

16. SECURITY CLASSIFICATION OF:			17. LIMITATION OF ABSTRACT	18. NUMBER OF PAGES	19a. NAME OF RESPONSIBLE PERSON USAMRMC
a. REPORT U	**b. ABSTRACT** U	**c. THIS PAGE** U	UU	49	**19b. TELEPHONE NUMBER** (include area code)

Table of Contents

1.0   INTRODUCTION

The overall goal of this project is to develop an experimentally validated computational model of the eye and apply the model to evaluate the stresses and deformations incurred by the eye-wall and critical ocular components from blast overpressures, and to investigate the interaction between the standard issue eye armor and the blast wave, and its effect on the mechanical loading of the eye. The model will be developed based on the following working hypotheses. 1) The anisotropic mechanical properties of the cornea and sclera as derived from the collagen structure, are critical to modeling the interaction of the blast wave and the globe. 2) The mechanical behavior of the cornea and sclera under dynamic (high-rate) loading is significantly different than the under qua-sistatic (slow-rate) loading. 3) The surrounding environment of the globe, including the extraocular tissues of the orbit and bony facial features is important in determining the effects of blast loading on the eye. In this second year of the project, we focused on developing a computational model to assess the effects of facial features and deformability of ocular tissues on the blast impact. In addition, we have made significant progress towards developing a constitutive model for the stress response of the cornea and sclera that includes the anisotropic effects of the collagen fiber structure. Moreover, we have begun developing analysis methods for the dynamical inflation experiments. These accomplishments are important steps in examining all three hypotheses.

2.0   BODY

2.1 Computational model to investigate effect of facial features and orbital tissue properties on blast wave loading on the eye.

This section presents a computational model of the human eye that takes into account the propagation of the wave and the associated deformation of the soft tissue of the eye and orbit. The objective of this study was to evaluate the influence

of facial features on blast wave loading on the human eye, to simulate deformation of the globe arising from realistic pressure loadings, and to characterize the time-history of the intraocular pressure (IOP), internal stresses, and deformations caused by the propagating blast wave. The result of this study has been submitted for publication and the submitted manuscript is included in the Appendix of this report.

The model involves three-dimensional geometries, moving structure boundaries within a fluid domain, and large flow-induced deformations of the structure. The flow field around the structure is compressible and pressure fields on the structure are non-uniform and highly transient. The modeling of the structure involves geometric and material nonlinearity. The coupled fluid-structure interaction (FSI) solver uses the following methods: (1) finite difference compressible flow solver for the propagation of the blast wave, (2) finite element elastodynamic solver with finite deformation of the globe, and (3) a sharp-interface immersed boundary method for fluid-structure interaction. The flow computations were performed on an Eulerian grid while the immersed structural surfaces were tracked in a Lagrangian framework. The detail development of each method is provided for in the Appendix.

2.1.1 Finite Element Models of the Human Face and Eye

To characterize pressure loading on the eye, we first modeled the interaction of the blast wave with a rigid (non-deformable) finite element model of the human head. The original head model, including the skin and skeletal structure among other anatomical components, was developed by Zygote Media Group, Inc.©[1]. This 3D triangular surface mesh was modified at the US Army Research Laboratory (ARL) using a suite of advanced mesh processing software, and quadratic edge decimation to form a smooth, manifold surface. Altair HyperMesh©, a finite element pre-processor, was used to convert the surface to a volumetric finite element tetrahedral mesh [2]. In this development, the skin was meshed through to the skull; therefore, nodes are shared at the interface. The skin mesh, referred to as the "skin model" in the following developments, is shown in Figure 1A. The skin model was scaled to the dimensions of a specific 21 year old male (similar to 50 percentile

male) to match the orbital width and orbital height as given in Weaver et al. [3]. The interpupillary distance of this subject was measured as 68.3 mm. The dimensions of the skin model are shown in Figure 1B,C.
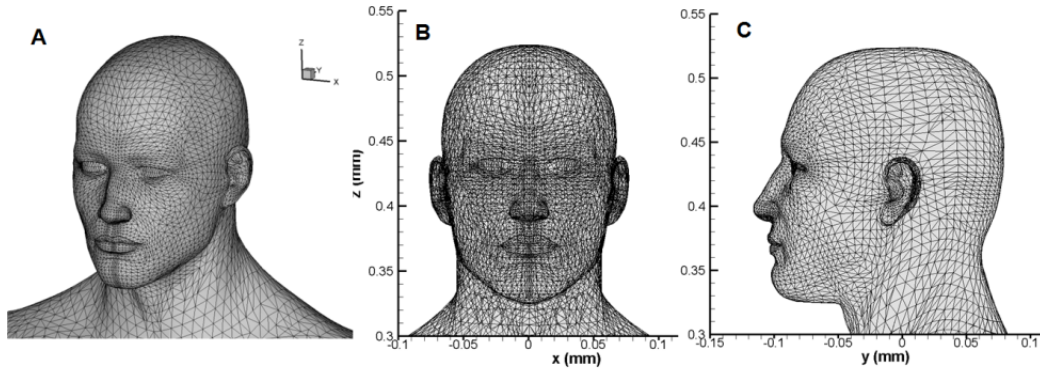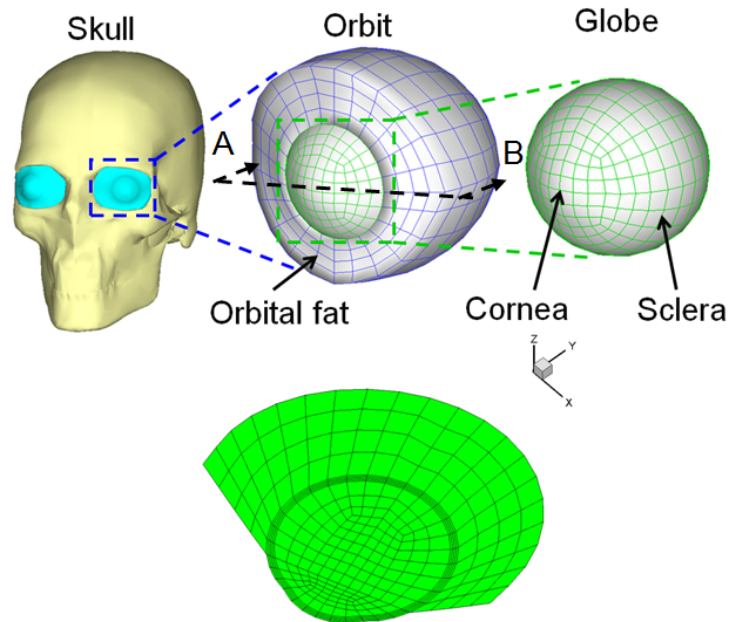

Figure 1: FE mesh of the skin model

To characterize the deformation of the globe resulting from the blast wave, we considered the skull as a rigid structure (Figure 2). The eyelid and skin were neglected in this model, which is referred to as the "skull model".

Cross section of the orbit (Section AB)

Figure 2: Skull model: FE model of the skull, orbit and the globe used in investigating the biomechanical response of the globe.
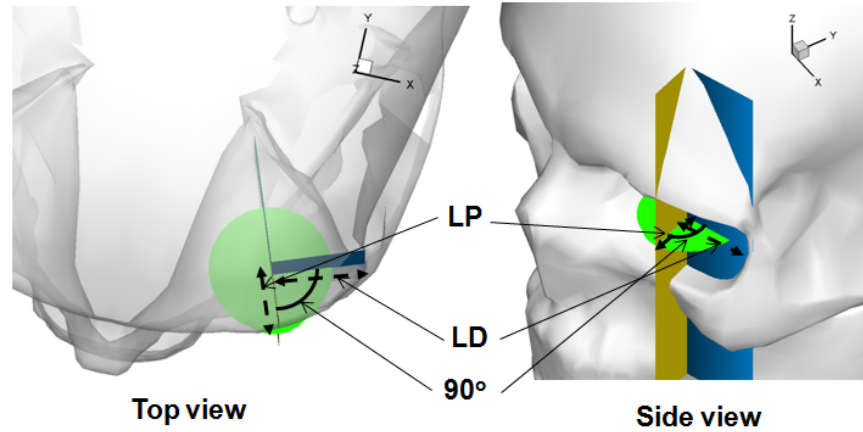

Figure 3: Definition of Lateral eye protrusion (LP) and lateral distance (LD).

The model of the globe was constructed to fit within the orbit of the skull as shown in Figure 2, based on the anatomical measurements obtained using CT scans by Weaver et al. [3]. Two parameters, namely the lateral eye protrusion (LP) and the lateral distance (LD), were used by Weaver et al. [3] to characterize the anatomical measurements of different subjects. The anterior–posterior axis was rotated in the axial plane of the globe with maximum eye protrusion until it was aligned with the cornea and the center of the optic canal. A normal axis to the anterior–posterior axis was drawn on the edge of the lateral orbital rim ([3], Figure 2). Lateral eye protrusion (LP) and lateral distance (LD) are defined as the distance of the cornea to the axes intersection and distance of axes intersection to the lateral orbital rim, respectively. To place the globe in the orbit, LP and LD values were matched as in Weaver et al. [3] for a specific 21 year old male (similar to 50 percentile male). The anthropometric parameters are given in Table 2.

Anatomical parameter	Value (mm)
Globe diameter	25.0
Orbital width, OW	36.0
Orbital height, OH	29.9
Lateral eye protrusion, LP	12.0
Lateral distance, LD	19.0
Interpupillary distance, IPD	68.3

Table 1: Anatomical parameters used in skin and skull model

The finite element mesh of the globe was created in CUBIT©, a geometry and mesh generation toolkit developed at Sandia National Laboratories [4]. The mesh is composed of linear hexahedral elements. The globe included a corneo-scleral shell and a space-filling, homogeneous internal solid (hereafter referred to as "inner solid") in lieu of vitreous and aqueous humor (Figure 2). The model did not include internal ocular components, namely, lens, zonules, and ciliary muscle. The diameter of the globe was taken as 25 mm [5] and its cross-section was comprised of two spherical geometries, namely, the anterior and the posterior chamber. The posterior chamber represented the sclera with an inner and outer radius of 12 and 12.5 mm, respectively. The anterior chamber represented the cornea, formed by a 7.8 mm radius circle whose center was offset by 5 mm from the center of the posterior chamber [5]. The outer and inner radii of the cornea were 7.8 and 7.3 mm, respectively. As a first approximation, the thickness of the corneo-scleral shell was considered uniform with a value of 0.5 mm. The globe was embedded in a cone of a space-filling, homogeneous solid (hereafter referred as "outer solid") representing the extra-ocular tissues and orbital fat (Figure 2). The stiffer extra-ocular eye muscles and internal components such as the lens, retina, and optic nerve head were not represented explicitly in this model. The attachment point of the orbital fat on the globe was determined from the measurements for a healthy 25-year-old female, reported by Schutte et al. [6].

2.1.2   Material properties

In our model, the bulk modulus (K) and density (ρ) of the internal solid were based on the respective average values of the aqueous and vitreous humor. The densities of the aqueous and vitreous humor were reported as 1003 and 1009 kg m-3 respectively [7], and the density of the internal solid was taken as the average value (1006 kg m-3). The speed of sound was reported as 1481-1525 m/s in aqueous at 25.5oC and as 1523-1532 m/s in vitreous at 37oC [7]. We took the average speed of sound in aqueous and vitreous, 1503 m/s, in the internal solid [5]

to calculate the bulk modulus as 2.272 × 103 MPa. The shear modulus of the internal solid was taken as 7 Pa, from the quasi-steady measurements of the shear modulus of bovine vitreous in Ref. [8]. The density of the corneo-scleral shell was taken as 1400 kg m-3 [5]. The bulk modulus of the corneo-scleral shell was taken as 3.5706× 103 MPa, which is based on the measured speed of sound in the sclera, 1597 m/s [9]. The dynamic shear modulus (G) of the corneo-scleral shell was taken as 1 MPa from the low-strain rate measurements of Bisplinghoff et al. [10] for the sclera. The low-strain rate values were chosen to be consistent with the available properties for the vitreous and extraocular tissues. The effect of the scleral shear modulus on the deformation of the globe will be examined as a parameter study in Section 3.2.1. The material properties of the outer solid were taken as the properties reported for the orbital fat. The density and bulk modulus of the outer solid were assumed to be equal to that of water [11-13] and taken as 1000 kg/m3 and 2.202 × 103 MPa (assuming speed of sound in water as 1484 m/s), respectively. The shear modulus of the outer solid was taken as 500 kPa from the measurements in Ref. [14]. The properties for the different components are summarized in Table 2.

Material	ρ (kg m^{-3})	K (MPa)	G (Pa)
Innersolid	1006	2.272×10^3	7
Corneo-scleral shell	1400	3.571×10^3	1×10^6
Outer solid	1000	2.202×10^3	5×10^5

Table 2: Material parameters used in the model

2.1.3 Modeling the TNT blast wave

The explosion of TNT produces a mixture of gases in the form of a "fireball" with high temperature and velocities [15]. McNesby et al. [15] measured the shock front velocity and temperature for an unconfined explosion of 2 kg TNT charge. We applied the measured velocity and temperature of the shock front from McNesby et al. [15] as an initial condition for the simulations at a radial distance of 1.8 m from the center of the explosion. The pressure of the shock-front for unconfined TNT explosions was well-documented by Kingery and Bulmash [16]. This data was later revisited by Swaidak [17] and is available in the form of scaled distance and mass of

the TNT. It has been widely accepted by researchers and the fitted curves have been implemented in the ConWep code of ARL and LS-DYNA. We applied the pressure measured for the shock front generated by a 2 kg TNT explosion at 1.8 m from the center of the explosion [16, 17]. The Gaussian profiles of the initial pressure and velocity are shown in Figure 4A and the initial temperature for the shock wave is shown in Figure 4B. The initial condition elsewhere in the computational domain was set to zero for velocity, and ambient value for the pressure and temperature.
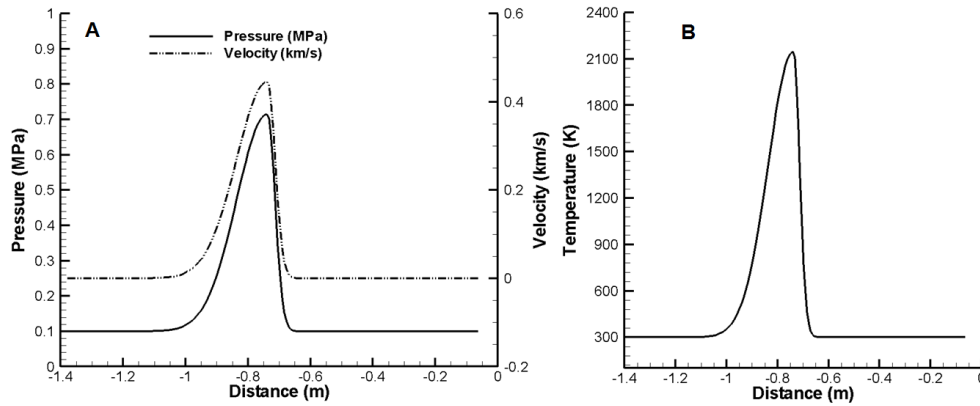

Figure 4: Initial conditions for the pressure, velocity and temperature.

2.1.4 Results

We considered a 2 kg TNT explosion in front of the face at a distance of 2.5 m (Figure 5). These parameters are based on the conditions of field tests for blast exposure, conducted by the US Army Research program [15].
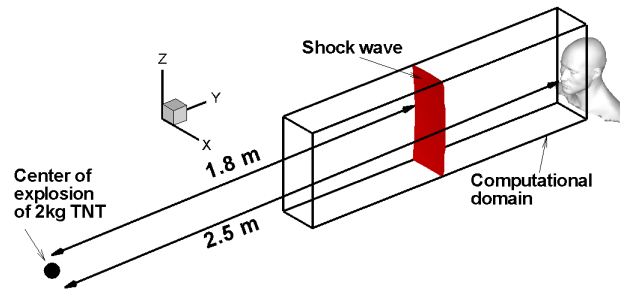

Figure 5: Simulation set up

To simulate the effects of facial features on blast wave reflections around the eye, the skin and all facial features including the eye were treated as rigid structures. The flow fields in the sagittal plane obtained by the fluid-structure interaction simulations are shown in Figure 6A. There were extensive reflections of the blast wave by the nasal and brow ridges. Together, they formed a reflector that focused the incident blast wave on the eye (Figure 6A). This effect allows a planar blast wave with a pressure p just before impacting the face to apply a peak pressure of 4p (1.4 MPa) on the eye during the impact. These reflections also produced an asymmetric pressure loading on the eye (Figure 6B) that was higher nearer to the nasal bone than the zygomatic bones. Figure 7 shows the time-variation of the pressure on the numerical probes A, B and C shown in Figure 6B. The peak pressure at probe B was around two times higher than the pressures at probes A or C, which confirms the asymmetric nature of pressure loading. The time-scale in Figure 7 further illustrates the highly transient and asymmetric nature of the pressure loading developed from blast wave interactions. The duration of pressure loading on the face was less than 1 ms (Figure 7), which is 300 times faster than the blink of the eye ($\sim$ 300 ms) [18].
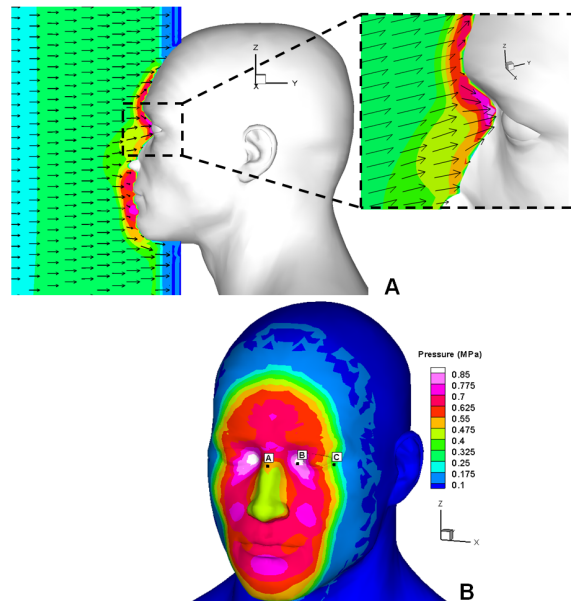

Figure 6: (A) Flow field and pressure contours are shown in sagittal plane. Zoomed in view of the brow area is shown to illustrate the blast-wave reflections (B)

Pressure contours on the face at the instance of the maximum pressure loading during the impact the blast wave.
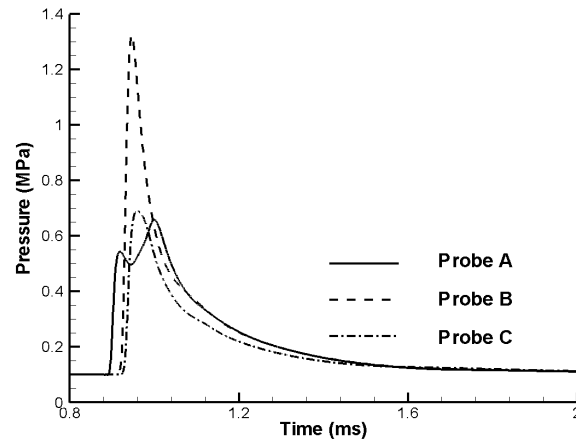

Figure 7: Comparison among time-varying pressures at probes A, B and C shown in the Fig 1B.

The influence of the location of the explosion was evaluated for a 2 kg TNT explosion on the ground at a distance of 2.5 m (Figure 8). Simulations of the blast on the ground suggested a similar asymmetric pressure loading on the eye as described in previous section. The peak pressure decreased by 40% for the explosion on the ground compared to that in front of the face.
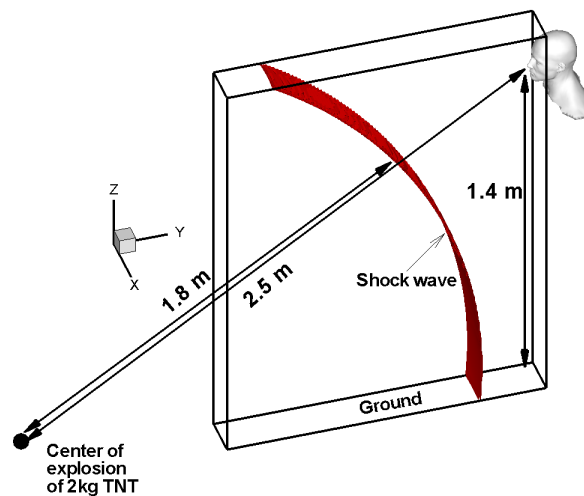

Figure 8: Initial condition of the simulation for influence of blast location.
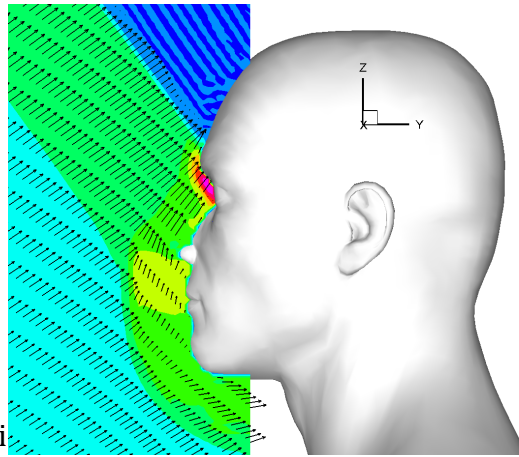
Figure 9: Flow fi... ...n sagittal plane.

The flow field shown in Figure 9 illustrates that the nasal and brow ridges do not act as an effective reflector of the incident wave in this case.

The skull model described in section 2.2.1 was used to evaluate the deformation response of the eye to the incident blast wave. All deformable solids, namely, internal solid, corneo-scleral shell and outer solid were treated as neo-Hookean quasi-incompressible solids in the structure model. The calculated peak pressure loading on the skull model was 30% lower as compared to the skin model. In the skull model, removing the skin layer decreased the brow protrusion and the lower cartilaginous part of the brow, which decreased the wave reflections on the eye. Hence, the peak pressure was lower than for the skin model. The skull model also exhibited asymmetric pressure loading on the eye. We examined the question of whether the pressure loading on the eye changes due to globe deformation, and determined that globe deformation had a negligible effect (less than 1%) on the loading for these cases.

The time-varying maximum principal stress (s1) of the corneo-scleral shell and intra-ocular pressure (IOP) are plotted in Figure 10A and s1 as well as IOP increased overall with time in addition to their periodic behavior. The overall increase was due to the time-varying pressure loading boundary condition and the periodic behavior of the stress and IOP can be explained by the wave propagation inside the orbit as follows. The blast wave travels inside the globe and the outer solid and becomes scattered when contacting the bony wall of the orbit. This

induces a periodic behavior of the intra-ocular pressure. The pressure contours in the transverse plane are shown in Figure 10B. The pressure was calculated as the mean of the three components of the principal stress. In Figure 10B, the highest pressure can be noticed near the orbital wall due to the wave scattering by the orbital wall. We note that the pressure is highest in the posterior region inside the inner solid. The grid points (red dots) where the IOP exceeded 0.35 MPa at 1.52 ms are shown in the inset of Figure 10A. The contours of the von Mises stresses in the transverse plane are plotted in Figure 10C, in which the largest von Mises stresses appeared in the sclera near the limbus. Due to asymmetric pressure loading the globe distorted relative to the orbital tissue and resulted in significant distortion of the sclera (Figure 10C).
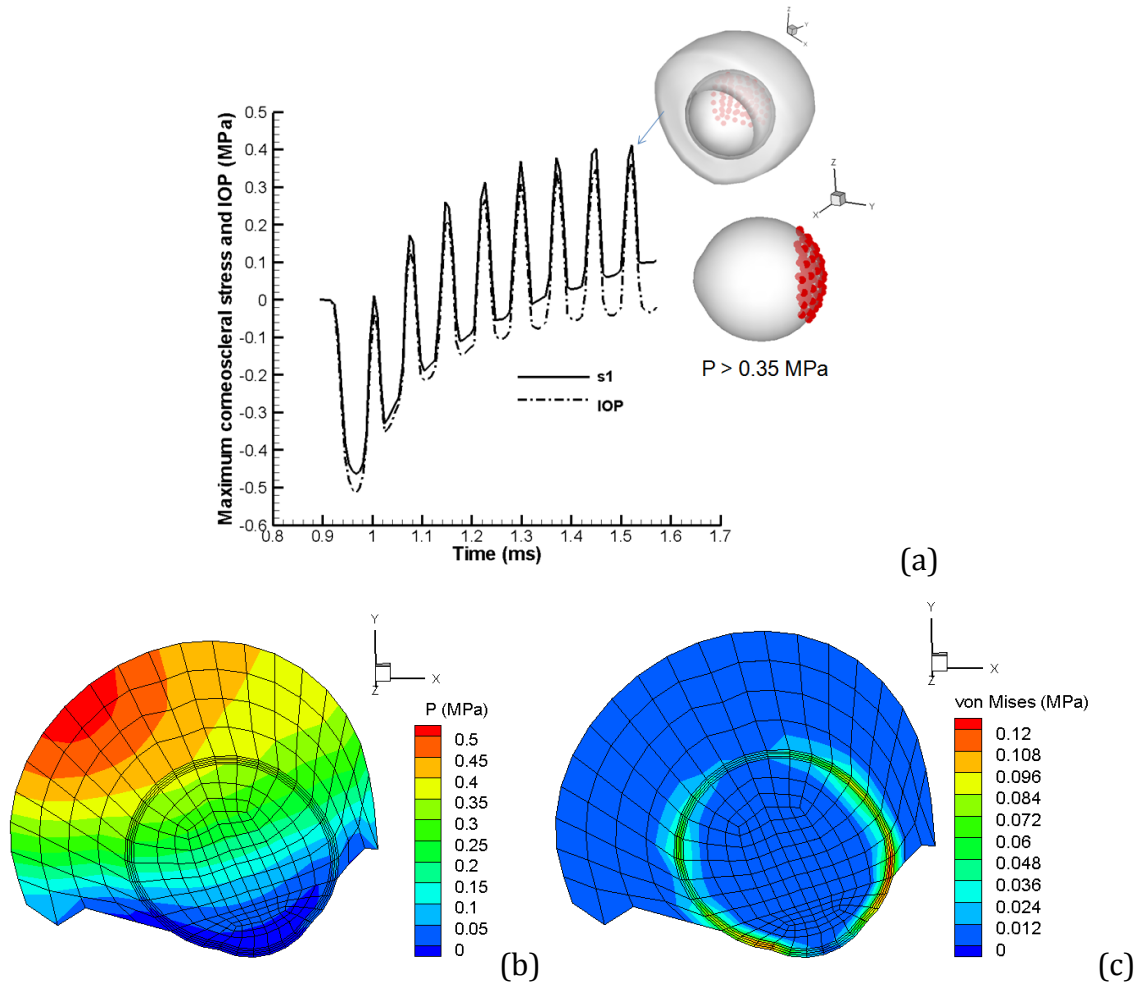

Figure 10: (a) Time-varying corneoscleral principal stress (s1) and maximum intraocular pressure (IOP) (b) Maximum pressure in the transverse plane of the

orbit. Distortion of the globe due to the blast wave is shown by the deformed mesh. (c) von Mises stress shown in the transverse plane, which is the largest in the sclera near limbus.

2.1.5 Discussion: implictions for eye injury

As shown in Figure 15A for the baseline case, the maximum IOP inside the globe reached 0.42 MPa, corresponding to around 3000 mm Hg, which is two orders of magnitude larger than the 15 mm Hg physiologic IOP for a healthy eye. The von Mises stresses were calculated largest in the sclera wall at the site of muscle attachments, which indicates significant muscle tearing or rupture inside the eye. We assessed the risk of eye injury using the functions published by Duma and Kennedy [19]. These injury risk functions were reported using measurements for blunt impact on the eye by a projectile. Recently, Alphonse et al. [20] calculated the injury risk for an increased IOP using correlation between the projectile normalized energy and the IOP by Duma et al. [21]. The calculated percentage of injury risks corresponding to the maximum IOP value 0.42 MPa for our simulation are around 98%, 14%, 0%, 0%, 0.02% respectively, for corneal abrasion, hyphema, lens dislocation, retinal damage and globe rupture. We summarize recent relevant clinical and experimental studies of primary ocular blast injury to provide context for our numerical data and injury risk analysis. Cockerham et al. [22] studied combat veteran in-patients (n = 46) with documented blast-induced traumatic brain injury in Iraq and Afghanistan. The closed-eye injuries such as corneal abrasion, vitreous haemorrhage, retinal detachment and optic nerve atrophy were found in 43% of the patients and it was noticed that patients outside the military vehicles had higher levels of ocular injury than did those situated within military vehicles [22]. These authors attributed this to closer proximity to the blast source, with attendant high blast overpressure, and the protective effect of armoured vehicles against blast waves and fragmentation. Hines-Beard et al. [23] reported primary ocular blast injury on mice, which were exposed to a maximum of 0.21 MPa blast pressure. In these experiments, increased ocular damage was reported with increased blast pressures and the following closed eye injuries were reported: corneal edema, corneal abrasions, and optic nerve avulsion.

2.2 Dynamic Inflation Experiments

We have designed and built a shock tube setup coupled with full field displacement measurements to characterize the mechanical behavior of the cornea and sclera at high pressure rates representative of primary blast conditions. The idea behind the dynamic inflation experiments is to record the dynamic pressure and full field displacement history at various levels of pressure. We previously described the design and validation of the shock tube in the FY11 Annual Report. A schematic of the shock tube setup for dynamic inflation experiments is shown in Figure 11. The shock tube, a specimen holding fixture and 2 high-speed imaging cameras are the components of the setup.
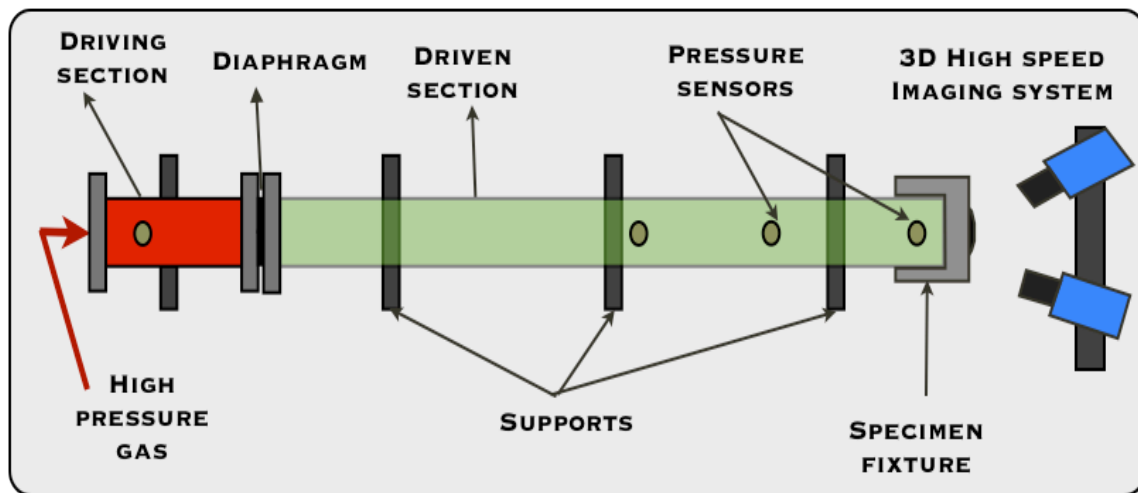

Figure 11: Schematic of a shock tube setup for dynamic inflation experiment.

In FY12, work has focused on understanding the effect of inertia on the evolution of the stress state of the membrane specimen subjected to dynamical inflation. This is necessary to determine the stress response of the corneal and sclera specimens under dynamic inflation. We performed a series of tests on an initially flat elastomeric membrane. The membrane was composed of Sylgard-184, which is a silicone elastomer (trademark of Dow Corning) with well known mechanical properties. Figure 12 plots the out of plane displacement of the top surface for a cross-section of the central region of the membrane measured by DIC. Also plotted are ellipse fits of the deformed surface that were used to calculate the curvature of the deformed membrane at the apex. The membrane appears to

deform rigidly with negligible curvature. The curvature develops at the edge of the specimen and travels radially inwards towards the apex. Figure 13A shows a plot of the principal in-plane Green-Lagrange strain at the apex of the specimen. The strain field was calculated from the gradient of the displacement field measured by DIC. The apex does not deform until 0.4 ms, after which both strain components increase exponentially with time. Figure 13A plots the pressure as a function of apex displacement, measured by internal pressure gages near the specimen.   The results show a flat pressure-displacement response. In contrast, pressure increases with apex displacement for quasistatic inflation.
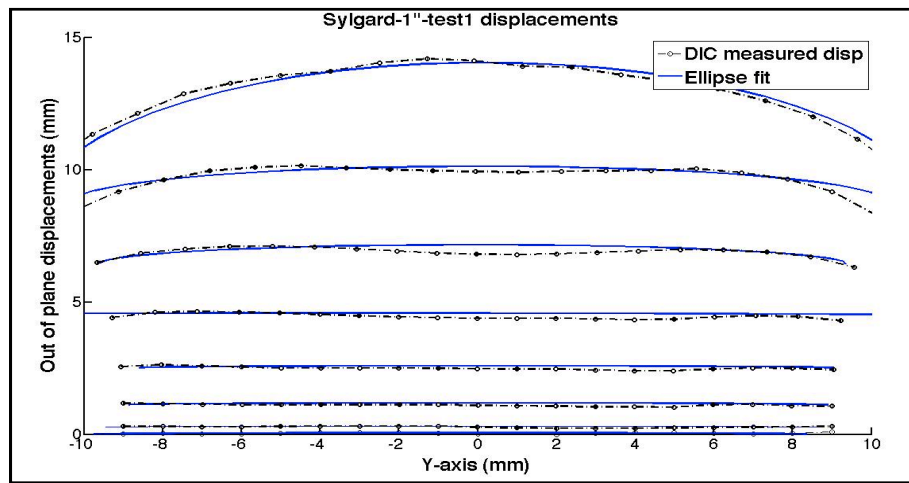

Figure 12. The time evolution of the out-of-plane displacement response plotted for a line *x=0* for the Sylgard membrane undergoing dynamic inflation.

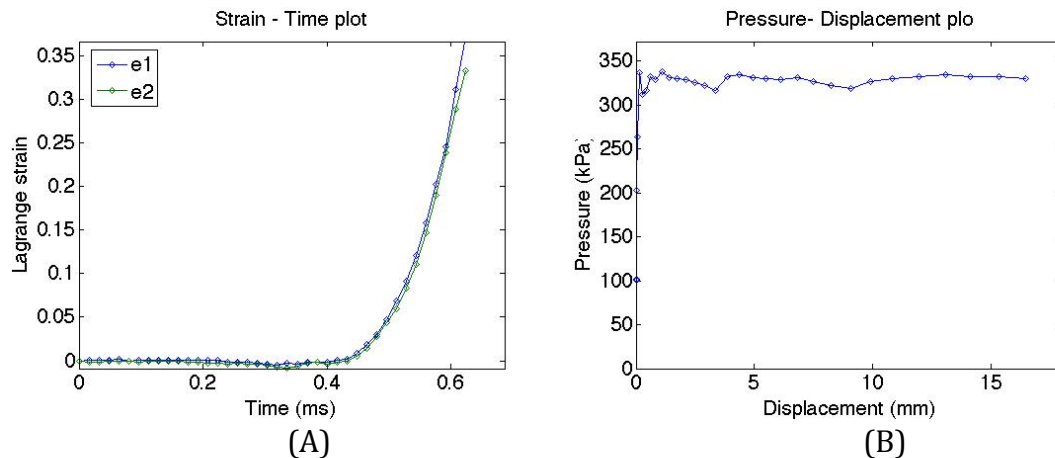(A)   (B)

Figure 13 (A) The principal in-plane strain response with time at the apex of the inflating membrane, and (B) the pressure displacement response for the apex.

To understand the pressure-displacement response, we performed a finite element simulation of the dynamic inflation experiments. A ramp-hold pressure loading was applied to the inner surface of the membrane, where the rise time and pressure level was taken from pressure measurements of the shock tube experiments. Figure 14 shows the deformed configuration of the membrane shortly after the pressure loading reached a constant value. The simulation shows that dynamic pressurization sets up a bending wave that travels radially from the clamped boundaries to the apex. The central region of the membrane displaces vertically and remains flat until the bending wave passes through the region setting up the equilibrium curvature. In FY13, we will continue the computational study of the response of a flat membrane and ellipsoidal dome, geometry representative of the cornea and sclera, to dynamic inflation. The results of the studies will guide the development of a stress analysis for the experiments. In addition, we will further develop the dynamic inflation experiments to characterize the properties of porcine cornea and scleral cups. This task will involve development of speckling methods that are robust enough to withstand the internal blast loading and provides sufficient resolution of the DIC measurements for local anisotropy.
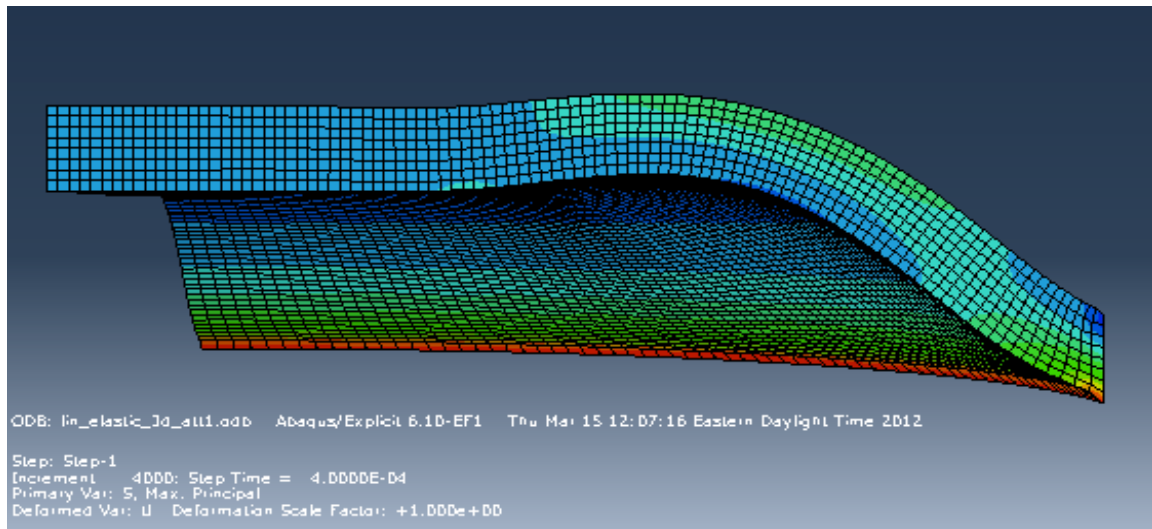

Figure 14 Finite element simulation of an initially flat membrane subjected to a dynamic constant pressure loading on the internal surface.

3.0   KEY RESEARCH OUTCOMES

1. Built a shock tube system with digital image correlation (DIC) setup to perform dynamic inflation experiments of ocular tissues and blast experiments on the globe.

2. Validated the shock-tube design by comparing theoretical and measured shock pressures.

3. Measured the accuracy of the DIC displacement measurements for both quasistatic and dynamic test systems.

4. Developed a method for strain calculation of DIC displacement measurements.

5. Performed a preliminary dynamic inflation experiment on bovine cornea and porcine sclera.

6. Developed a fluid-structure interaction solver that involves compressible flow and large deformation.

7. Developed computational model of human eye and applied the model to study the effect of facial features and tissue properties on determining the blast pressure loading on the eye.

8. Began developing a microstructure-based constitutive model to describe the nonlinear, anisotropic stress response of the tissues.

9. Measured the anisotropic collagen orientation distribution of the posterior human sclera.

4.0   Reportable Outcomes

1. Bhardwaj R., Ziegler K, Seo J. H, Ramesh K.T., Nguyen T.D. (2012) "A Computational Model of Blast Loading on the Human Eye", Biomechanics and Modeling in Mechanobiology, submitted October 2012.

2. Ziegler K.A., Nguyen T.D. "Modeling study investigating the depth-dependent fiber-reinforcement in corneal tissue", Poster Presentation Summer Bioengineering Conference, June 20-23th, 2012, Fajardo Puerto Rico.

3. Bhardwaj R., Ziegler K. A., Nguyen T. D. "Blast Wave Reflections on the Human Eye", Poster Presentation: ARVO, Fort Lauderdale, FL, May 9, 2012.

4. Ziegler K.A., Yatnalkar R.S., Ramesh K.T., Nguyen T.D. "Modeling Study for the Design of An Innovative Composite Membrane Inflation Test", Poster Presentation: Summer Bioengineering Conference, June 22-25th, 2011, Farmington Pennsylvania.

5. Yatnalkar R.S., Ziegler K.A., Ramesh K.T., Nguyen T.D., "Development of a shock tube to study primary blast effects in ocular blast injuries", Conference presentation: Society of Experimental Mechanics, June 14th, 2011, Uncasville, CT.

4.0   CONCLUSION

The main focus over the second year of the project was to develop a fluid-structure interaction solver and a computational model of the human eye to examine the effects of facial features and tissue properties on the blast pressure loading. The results show that the nasal and brow ridge act as reflector that focuses the pressure loading on the eyes. This also generated an asymmetric pressure loading on the eye that leads to gross distortion of the globe within the extraocular tissues. The deformation of the globe had little effect on the blast pressure loading on the eye. We are currently developing an anisotropic hyperelastic constitutive model for the tissues of the eye wall to determine the effects of collagen structure on the dynamic response of the tissues. This will further advance the accuracy of the computational model of the eye.   We continued to make progress on the development of the dynamic inflation test. Work in the second year focused on understanding the evolution of the stress and strain fields from dynamic pressurization. This is needed to develop a stress analysis for the tests, which is

ultimately needed to determine mechanical properties of the tissues. These accomplishments add to the scientific knowledge base for ocular biomechanics under blast conditions as well as the broader knowledge base of computational biomechanics and experimental mechanics.

For FY13, we plan to complete the development of the analytical methods for the dynamic inflation tests. Furthermore, we will apply the method to measure the dynamic stress-strain response and rupture conditions of human cornea and sclera. For the modeling effort, we will complete development of a stress-strain model for the cornea and sclera that incorporates the anisotropic lamellar structure and crimped fibril structure. The parameters of the model will be determined from the inflation measurements. The constitutive model will be integrated into the current computational model for the eye. We will also further develop the computation model to include important intraocular components, such as the lens, retina, and optic nerve head. The computational model will be applied to investigate the deformation and stress fields in the internal ocular components. Furthermore, we will apply the model to simulate the effect of protective eye equipment on blast wave loading on the eye. These simulations will ultimately help to design next generation protective eyewear, which could drastically mitigate blast injuries.

References

[1]Zygote Media Group, Inc is a developer company for computer-generated 3D graphical software, and of late has specialized in the enhanced visualization of the human anatomy (http://www.zygote.com/).

[2]Altair HyperMesh is a high-performance finite element pre-processor that provides an interactive environment for mesh development and analysis (http://www.altairhyperworks.com/).

[3] AA Weaver, KL Loftis, JC Tan, SM Duma, JD Stitzel (2010) "CT based three-dimensional measurement of orbit and eye anthropometry," Invest Ophthalmol Vis Sci. Vol 51(10), p 4892-7.

[4]CUBIT is a geometry and mesh generation toolkit developed at Sandia National Laboratories (http://cubit.sandia.gov/).

[5]Stitzel J, Duma S, Herring I, Cormier J. (2002) "A Nonlinear Finite Element Model of the Eye with Experimental Validation for the Prediction of Globe Rupture," Stapp Car Crash Journal, Vol. 46, pp. 81-102

[6]Schutte S, van den Bedem SPW, van Keulen F, van der Helm FCT, Simonsz HJ. (2006) Finite-element analysis model of orbital biomechanics. Vision Res. Vol 46, p 1724.

[7]Duck FA (1990). Physical Properties of Tissue: A Comprehensive Reference Book. London.. Academic press, p 77-78, 138

[8]Nickerson CL, Park J, Kornfield JA, Karageozian H. (2008). Rheological properties of the vitreous and the role of hyaluronic acid. J. Biomechanics. Vol 41 p 1840

[9]Bereiter-Hahn J. Advances in acoustic microscopy. Berlin, Germany: Springer; 1995. Probing biological cells and tissues with acoustic microscopy.

[10]Bisplinghoff JA, C McNally, SJ Manoogian and SM Duma. (2009).Dynamic material properties of the human scleraJ. Biomechanics. Vol 42 p 1493.

[11]Computer modelling study of the mechanism of optic nerve injury in blunt trauma, S Cirovic, R M Bhola, D R Hose, I C Howard, P V Lawford, J E Marr, M A Parsons, Br J Ophthalmol 2006;90:778–783

[12]Power, E. D. 2001 A nonlinear finite-element model of the human eye to investigate Ocular injuries from night vision goggles. M.S. thesis, Virginia Polytechnic Institute and State University, Virginia.

[13]Modelling of orbital deformation using finite-element analysis Jehad Al-Sukhun, Christian Lindqvist and RistoKontio, J. R. Soc. Interface (2006) 3, 255–262

[14]Schoemaker I, Hoefnagel PPW, Mastenbroek TJ, et al. Elasticity viscosity and deformation of the retrobulbar fat in eye rotation. Invest Ophthalmol Vis Sci 2004;45(suppl 2):U651

[15]KL McNesby, BE Homan, JJ Ritter, Z Quine, RZ Ehlers, BA McAndrew (2010). After burn Ignition Delay and Shock Augmentation in Fuel Rich Solid Explosives. *Propellents, Explosives andPyrotechnics*, Vol 35, pp 57 – 65

[16]CN Kingery, G Bulmash (1984).Airblast Parameters from TNT Spherical Air Burst and Hemispherical Surface Burst, Defence, Tech. Rep. Report ARBL-TR-02555, U.S. Army BRL, Aberdeen Proving Ground, MD.

[17]Swisdak, M.: Simplified kingery airblast calculations. In: Minutes of the 26th DOD Explosives Safety Seminar (1994). Available at http://www.dtic.mil/cgi-bin/GetTRDoc?AD=ADA526744

[18]Tsubota K, Hata S, Okusawa Y, Egami F; Ohtsuki T; Nakamori K, Quantitative Videographic Analysis of Blinking in Normal Subjects and Patients With Dry Eye, *Arch Ophthalmol*. 1996; Vol 114(6):715-720.

[19]Kennedy E and Duma S (2011). Final report: Eye Injury Risk Functions for Human and FOCUS Eyes: Hyphema, Lens Dislocation, and Retinal Damage, Technical report, U.S. Army Medical Research and Material Command Fort Detrick, Maryland. Available at http://www.facstaff.bucknell.edu/eak012/Reports_n_Papers/Eye_Injury_Risk_Functions_for_Human_and_FOCUS_Eyes--FinalReport_W81XWH-05-2-0055--July2011Update.pdf(Accessed July 23, 2012).

[20]Alphonse VD, Kemper AR, Strom BT,Beeman SM, Duma SM, (2012). Mechanisms of Eye Injuries From Fireworks, *JAMA*.Vol 308(1) p 33-34.

[21]Stefan M. Duma, Jill A. Bisplinghoff, Danielle M. Senge, Craig McNally, and Vanessa D. Alphonse, (2012) Evaluating the Risk of Eye Injuries: Intraocular Pressure During High Speed Projectile Impacts, *Current Eye Research,* Vol 37(1), 43–49, 2012.

[22]Cockerham, C.G., Rice, T.A., Hewes, E.H., Cockerham, K.P., Lemke, S., Wang, G., Lin, R.C., Glynn-Milley, C., 2011. Closed-eye ocular injuries in the Iraq and Afghanistan wars. New Engl. J. Med. 364, 2172-2173

[23]Hines-Beard J, Marchetta J, Gordon S, Chaum E, Geisert EE, Rex TS. A mouse model of ocular blast injury that induces closed globe anterior and posterior pole damage. Exp Eye Res. 2012 Jun;99(1):63-70. Epub 2012 Apr 7. PubMed PMID: 22504073.

---

[1]Zygote
[2]Altair
[3]Weaver_CT
[4]Cubit
[5] Stizel_2002
[6]Schuttle
[7] Duck
[8]Nickerson
[9]Bereiter
[10]Bisplinghoff
[11]Cirovic
[12] Power
[13] Al-Sukhum
[14]Schoemaker
[15]McNesby
[16]Kingerybulmash
[17]Swisdak
[18]Tsubota
[19]Keneddy
[20]Duma_JAMA
[21]Duma_riskfunc
[22]Cockerham
[23]Rex

A Computational Model of Blast Loading on The Human Eye

Rajneesh Bhardwaj[1], Kimberly Ziegler[2], Jung Hee Seo[2],K.T. Ramesh[2], Thao D. Nguyen[2,*]
Department of Mechanical Engineering,
[2]Johns Hopkins University, Baltimore, MD, 21218 USA
[1]Indian Institute of Technology Bombay, Mumbai, 400076 India
[*]Corresponding author (vicky.nguyen@jhu.edu)

Abstract

Ocular injuries from blast have increased in recent wars, but the injury mechanism associated with the primary blast wave is unknown. We employ a three-dimensional fluid-structure interaction computational model to understand the stresses and deformations incurred by the globe due to blast overpressure. Our numerical results demonstrate that the blast wave reflections off the facial features around the eye increase the pressure loading on and around the eye. The blast wave produces asymmetric loading on the eye, which causes globe distortion. The deformation response of the globe under blast loading was evaluated and regions of high stresses and strains inside the globe were identified. Our numerical results show that the blast loading results in globe distortion and large von Mises stresses in the sclera, which may increase the risk for muscle tearing and rupture.

1   Introduction

Ocular injuries from blasts have increased in recent engagements [1, 2]. Nearly 80% of ocular injuries suffered in the Iraq war were caused by blasts from munitions and improvised explosive devices (IEDs) [3, 4]. Such injuries are classified as primary and secondary injuries and are caused respectively by blast over pressures and fragments from debris [5]. Several factors are hypothesized to influence the severity of primary eye injury in the literature [6]: the high pressure shock front and the subsequent wave of lower sub-atmospheric pressure [7], threshold overpressure [6], and reflection of the shock wave by the orbit [8, 9, 10]. There is, however, a dearth of clinical data that could verify the hypotheses above and establish the mechanism of the injury. Measuring and assessing the influence of these factors is difficult because survivable primary blast injuries are likely accompanied by injuries from fragments and blunt-force trauma and are thus more difficult to distinguish and enumerate. Moreover, the severity of the blast injuries and distance of the tertiary care facility from the injury site means that often patients are unable to recount the injury event, and witnesses are unavailable. The same limitations hinder clinical studies of the effectiveness of current eye armor, developed for ballistic and laser protection, in preventing blast injuries.

A few computational models have been developed to study the effects of impact from fragments of comparable size to the eye (blunt impact). The 3D model of Uchio et al. [11] and the axisymmetric model of Stitzel et al. [12] focused on achieving physiologic geometric representations of the cornea, sclera, lens, ciliary body, choroid, retina, aqueous humor and vitreous humor. Neither model considered the extraorbital tissues and skull beyond applying a fixed boundary condition at the posterior surface. Both models idealized the material behavior of the ocular tissues as nearly incompressible, linear elastic, and isotropic, though the model of Stitzel et al. [12]

1

allowed for large deformations. Recognizing the important structural function of the eye-wall, Uchio et al. [11] developed a more representative nonlinear constitutive model for the stress response of the cornea and sclera. The material properties and failure strains of the cornea and sclera were measured from uniaxial strip tests under quasi-static (low rate) loading conditions. Stitzel et al. [12] employed a finite-element model to simulate the impact of BB pellets, baseballs, and foam projectiles on the cornea. The results showed the highest principal stresses occurred near the limbus for the impacting foam and near the equator for the baseball, which agreed with experiments [12]. In more recent work [13], the orbit and extraocular tissues were modeled using a chamber filled with a compliant material and threshold values of intraocular pressure (IOP) for globe rupture and peak values of stresses in corneoscleral shell were reported. Weaver et al. [14] evaluated eye injury due to blunt impact for different orbital anthropometries using a model of the globe developed in [12]. Their numerical results suggested the eye is more protected from impact with greater brow protrusion, less eye protrusion, and smaller orbital apertures, provided that the aperture is large enough to deter contact between the orbit and the eye [14]. Computational FE models have also been used to assess the injury to the orbit [15, 16] and the optic nerve [17] as a result of blunt object impact to the eye. To the best of our knowledge, there is no model in the literature which simulates the blast wave outside the eye and the associated deformation of the eye. To this end, we present a computational model that takes into account the propagation of the wave and the associated eye deformation (with consideration of extraocular tissues of the orbit). The objective of this study was to evaluate the influence of facial features on blast wave loading on the human eye, to simulate deformation of the globe arising from realistic pressure loadings, and to characterize the time-history of the intraocular pressure (IOP), internal stresses, and deformations caused by the propagating blast wave.

2 Methods

The methods used for the computational modeling of blast wave interactions with the eye are presented in this section. The modeling involves three-dimensional geometries, moving structure boundaries within a fluid domain, and large flow-induced deformations of the structure. The flow field around the structure is compressible and pressure fields on the structure are non-uniform and highly transient. The modeling of the structure involves geometric and material nonlinearity. We propose a coupled fluid-structure interaction (FSI) solver that uses the following methods:
- Finite difference compressible flow solver for the propagation of the blast wave
- Finite element elastodynamic solver with finite deformation of the globe
- Sharp-interface immersed boundary method for fluid-structure interaction

The flow computations were performed on an Eulerian grid while the immersed structural surfaces were tracked in a Lagrangian framework. In the following sections, we describe these three components of the modeling.

2.1 Flow solver

To resolve the propagation and scattering of a blast (shock) wave, we considered the full compressible Navier-Stokes equations for air. The equations are written in a conservative form as

$$\frac{\partial \rho}{\partial t} + \frac{\partial (\rho u_i)}{\partial x_i} = 0 , \tag{1}$$

$$\frac{\partial (\rho u_i)}{\partial t} + \frac{\partial (\rho u_i u_j)}{\partial x_j} + \frac{\partial p}{\partial x_i} - \frac{\partial \tau_{ij}}{\partial x_j} = 0 , \tag{2}$$

$$, \tag{3}$$

$$e = \frac{p}{\gamma - 1} + \frac{1}{2} \rho u_i u_i , \tag{4}$$

where ρ, u_i, p, and e are the density, velocity, pressure, and total energy, respectively, and τ_{ij} is the viscous stress, q_j is the heat flux, and γ is the specific heat ratio (1.4 for air). Equations (1-3) were spatially discretized by a sixth-order central compact finite difference scheme [18] and integrated in time using a four-stage Runge-Kutta method. An eight-order implicit spatial filtering proposed by Gaintonde et al. [19] was applied at the end of each time step to suppress high frequency dispersion errors. In order to resolve the discontinuity in the flow variables caused by a shock wave with the current non-dissipative numerical scheme, the artificial diffusivity method proposed by Kawai and Lele [20] had been applied. In this method, the viscous stress and heat flux are written as

$$\tau_{ij} = (\mu + \mu^*)\left(\frac{\partial u_i}{\partial x_j} + \frac{\partial u_j}{\partial x_i} \right) + \left(\beta^* - \frac{2}{3}\mu \right) \frac{\partial u_k}{\partial x_k} \delta_{ij} , \tag{5}$$

$$q_j = (\kappa + \kappa^*)\frac{\partial T}{\partial x_j} , \quad T = p/(\rho R) , \tag{6}$$

where μ and κ are the physical viscosity and thermal diffusivity, respectively, while μ^* is the artificial shear viscosity, β^* is the artificial bulk viscosity, and κ^* is the artificial thermal diffusivity. On the non-uniform Cartesian grid, these artificial diffusivities were adaptively and dynamically evaluated by

$$, \tag{7}$$

$$, \tag{8}$$

where C_μ, C_β, and C_κ are user-specified constants, c is the speed of sound, S is the magnitude of the strain rate tensor,

$$S_{ij} = \frac{1}{2}\left(\frac{\partial u_i}{\partial x_j} + \frac{\partial u_j}{\partial x_i} \right) , \tag{9}$$

3

Δx_k is the grid spacing, and over-bar denotes Gaussian filtering [21]. We used C_μ=0.002, C_β=1.0, and C_κ=0.01 as suggested in Kawai and Lele [20] and the fourth derivatives were computed by a fourth-order central compact scheme [18]. From equations (7) and (8), artificial diffusivities are significantly larger only in the region where the steep gradient of flow variables exists, and ensure numerical stability in that region.

2.2 Structural solver

The displacement vector $\mathbf{d}(\mathbf{x}, t)$ describes the motion of each point in the deformed solid as a function of space $\mathbf{x}$ and time t. The deformation gradient tensor F_{ik} can be defined in terms of the displacement gradient tensor $\dfrac{\partial d_i}{\partial x_k}$ as follows:

$$F_{ik} = \delta_{ik} + \frac{\partial d_i}{\partial x_k}, \tag{10}$$

where δ_{ik} is the Kronecker delta symbol, defined as follows:

$$\delta_{ik} = \begin{cases} 1, i = k \\ 0, i \neq k, \end{cases} \tag{11}$$

The right Cauchy green tensor is defined in terms of the deformation gradient tensor as follows:

$$, \tag{12}$$

The invariants of the right Cauchy green tensor are defined as follows:

$$I_1 = \lambda_1 + \lambda_2 + \lambda_3 \tag{13}$$
$$I_2 = \lambda_1\lambda_2 + \lambda_2\lambda_3 + \lambda_3\lambda_1,$$
$$I_3 = \lambda_1\lambda_2\lambda_3$$

where λ_i are eigen values of the right Cauchy green tensor. The strain-energy density function ψ of a neo-Hookean, quasi-incompressible solid is written as [22]:

$$, \tag{14}$$

where G and K are shear and bulk moduli and   . The Cauchy stress is given in terms of strain energy function ψ as follows:

$$\sigma_{ij} = \frac{1}{J}\frac{\partial \psi}{\partial F_{ik}} F_{jk}, \tag{15}$$

where J = det($\mathbf{F}$) denotes the volume change ratio. The governing equations for the structure are the Navier equations (momentum balance equation in Lagrangian form) and are written as:

$$, \tag{16}$$

where i and j range from 1 to 3, ρ_s is the density of the structure, d_i is the displacement component in the i direction, t is the time, $\boldsymbol{\sigma}$ is the Cauchy stress tensor and f_i is the body

4

force component in the *i* direction. The momentum balance equation was solved by finite elements using the Galerkin method for spatial discretization, which yielded the following system of ordinary differential equations for the nodal displacement vector **d**:

$$M \ddot{d}_{n+1} + K d_{n+1} = F_{n+1},$$
(17)

where *M* is the lumped mass matrix and *K* is the stiffness matrix. The Galerkin method was implemented in Tahoe©, an open-source, Lagrangian, three-dimensional, finite-element solver [23]. The central-difference method was used for the time integration, which resulted in an explicitly and conditionally stable second order scheme [24]:

$$d_{n+1} = d_n + \Delta t \, \dot{d}_n + \frac{\Delta t^2}{2} \ddot{d}_n$$
(18)
$$\dot{d}_{n+1} = \dot{d}_n + \frac{\Delta t}{2} \left(\ddot{d}_n + \ddot{d}_{n+1} \right),$$

The constraints of the time-step of the governing equations for the fluid and solid are different and are governed by the wave speed in the respective domain. In the present case, the wave speed inside the eye is larger than that in the ambient air (see Section 2.2.2) because of the higher wave speed in the water-like fluids (aqueous and vitreous humor) inside the eye. Thus, the time-step was chosen to resolve the longitudinal wave speed within the structure.

2.2.1 FE model of the orbit and the eye

To characterize pressure loading on the eye, we first modeled the interaction of the blast wave with a rigid (non-deformable) finite element model of the human head. The original head model, including the skin and skeletal structure among other anatomical components, was developed by Zygote Media Group, Inc.©[25]. This 3D triangular surface mesh was modified at the US Army Research Laboratory (ARL) using a suite of advanced mesh processing software, and quadratic edge decimation to form a smooth, manifold surface. Altair HyperMesh©, a finite element pre-processor, was used to convert the surface to a volumetric finite element tetrahedral mesh [26]. In this development, the skin was meshed through to the skull; therefore, nodes are shared at the interface. The skin mesh, referred to as the "skin model" in the following developments, is shown in Figure 1A. The skin model was scaled to the dimensions of a specific 21 year old male (similar to 50 percentile male) to match the orbital width and orbital height as given in Weaver et al. [27]. The interpupillary distance of this subject was measured as 68.3 mm. The dimensions of the skin model are shown in Figure 1B,C.
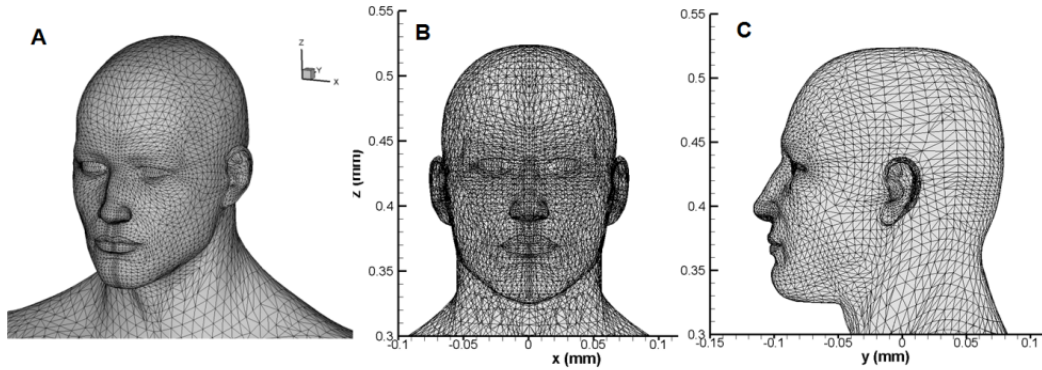
Figure 1: FE mesh of the skin model

To characterize the deformation of the globe resulting from the blast wave, we considered the skull as a rigid structure (Figure 2). The eyelid and skin were neglected in this model, which is referred to as the "skull model".
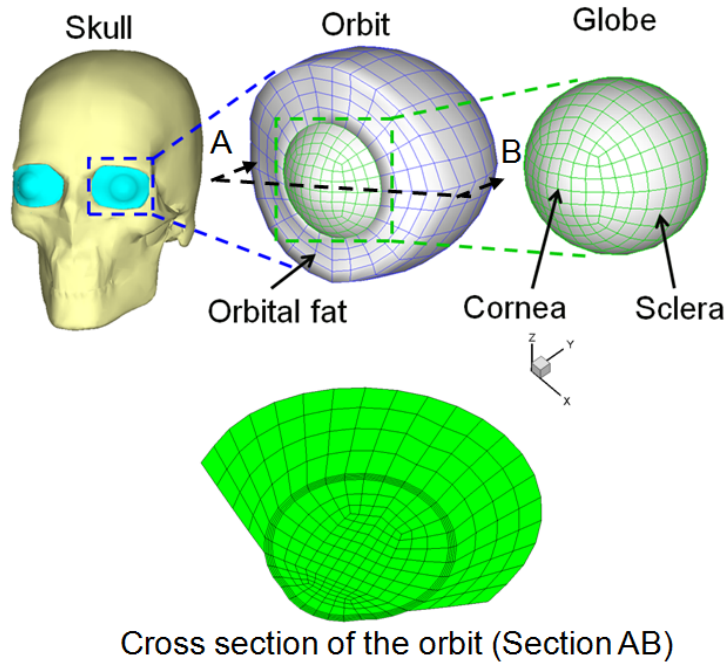

Cross section of the orbit (Section AB)

Figure 2: Skull model: FE model of the skull, orbit and the globe used in investigating the biomechanical response of the globe.
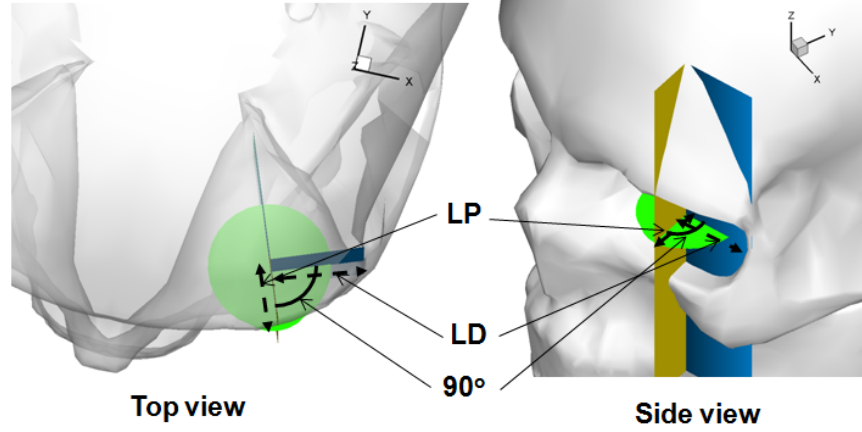
Figure 3: Definition of Lateral eye protrusion (LP) and lateral distance (LD).

The model of the globe was constructed to fit within the orbit of the skull as shown in Figure 2, based on the anatomical measurements obtained using CT scans by Weaver et al. [27]. Two parameters, namely the lateral eye protrusion (LP) and the lateral distance (LD), were used by Weaver et al. [27] to characterize the anatomical measurements of different subjects. The anterior–posterior axis was rotated in the axial plane of the globe with maximum eye protrusion until it was aligned with the cornea and the center of the optic canal. A normal axis to the anterior–posterior axis was drawn on the edge of the lateral orbital rim ([27], Figure 2). Lateral eye protrusion (LP) and lateral distance (LD) are defined as the distance of the cornea to the axes intersection and distance of axes intersection to the lateral orbital rim, respectively. To place the globe in the orbit, LP and LD values were matched as in Weaver et al. [27] for a specific 21 year old male (similar to 50 percentile male). The anthropometric parameters are given in Table 2.

Anatomical parameter	Value (mm)
Globe diameter	25.0
Orbital width, OW	36.0
Orbital height, OH	29.9
Lateral eye protrusion, LP	12.0
Lateral distance, LD	19.0
Interpupillary distance, IPD	68.3

Table 1: Anatomical parameters used in skin and skull model

The finite element mesh of the globe was created in CUBIT©, a geometry and mesh generation toolkit developed at Sandia National Laboratories [28]. The mesh is composed of linear hexahedral elements. The globe included a corneo-scleral shell and a space-filling, homogeneous internal solid (hereafter referred to as "inner solid") in lieu of vitreous and aqueous humor (Figure 2). The model did not include internal ocular components, namely, lens, zonules, and ciliary muscle. The diameter of the globe was taken as 25 mm [12] and its cross-section was comprised of two spherical geometries, namely, the anterior and the posterior chamber. The posterior chamber represented the sclera with an inner and outer radius of 12 and 12.5 mm, respectively. The anterior chamber represented the cornea, formed by a 7.8 mm radius circle whose center was

7

offset by 5 mm from the center of the posterior chamber [12]. The outer and inner radii of the cornea were 7.8 and 7.3 mm, respectively. As a first approximation, the thickness of the corneo-scleral shell was considered uniform with a value of 0.5 mm. The globe was embedded in a cone of a space-filling, homogeneous solid (hereafter referred as "outer solid") representing the extra-ocular tissues and orbital fat (Figure 2). The stiffer extra-ocular eye muscles and internal components such as the lens, retina, and optic nerve head were not represented explicitly in this model. The attachment point of the orbital fat on the globe was determined from the measurements for a healthy 25-year-old female, reported by Schutte et al. [29].

2.2.2 Material properties

In our model, the bulk modulus (K) and density (ρ) of the internal solid were based on the respective average values of the aqueous and vitreous humor. The densities of the aqueous and vitreous humor were reported as 1003 and 1009 kg m^{-3} respectively [30], and the density of the internal solid was taken as the average value (1006 kg m^{-3}). The speed of sound was reported as 1481-1525 m/s in aqueous at 25.5^{o}C and as 1523-1532 m/sin vitreous at 37°C [30]. We took the average speed of sound in aqueous and vitreous, 1503 m/s, in the internal solid [12] to calculate the bulk modulus as 2.272×10^3 MPa. The shear modulus of the internal solid was taken as 7 Pa, from the quasi-steady measurements of the shear modulus of bovine vitreous in Ref. [31]. The density of the corneo-scleral shell was taken as 1400 kg m^{-3} [12]. The bulk modulus of the corneo-scleral shell was taken as 3.5706×10^3 MPa, which is based on the measured speed of sound in the sclera, 1597 m/s [32]. The dynamic shear modulus (G) of the corneo-scleral shell was taken as 1 MPa from the low-strain rate measurements of Bisplinghoff et al. [33] for the sclera. The low-strain rate values were chosen to be consistent with the available properties for the vitreous and extraocular tissues. The effect of the scleral shear modulus on the deformation of the globe will be examined as a parameter study in Section 3.2.1. The material properties of the outer solid were taken as the properties reported for the orbital fat. The density and bulk modulus of the outer solid were assumed to be equal to that of water [34, 35, 36] and taken as 1000 kg/m^3 and 2.202×10^3 MPa (assuming speed of sound in water as 1484 m/s), respectively. The shear modulus of the outer solid was taken as 500 kPa from the measurements in Ref. [37]. The properties for the different components are summarized in Table 2.

Material	ρ (kg m^{-3})	K (MPa)	G (Pa)
Innersolid	1006	2.272×10^3	7
Corneo-scleral shell	1400	3.571×10^3	1×10^6
Outer solid	1000	2.202×10^3	5×10^5

Table 2: Material parameters used in the model

2.3 Fluid-structure interaction coupling

A partitioned approach was used to couple the flow and the structure solvers [38]. In this approach, flow and structure solvers are coupled such that they exchange data at each

time step (Figure 4A). In general, there are two coupling methods used in fluid structure interaction algorithms— explicit (or weak, one-way) coupling and implicit (or strong, two-way) coupling. As the name suggests, explicit and implicit coupling integrate the governing equations of the flow and the structure domain explicitly and implicitly in time. Explicit coupling is computationally inexpensive and may be subject to stability constraints, which depends on the structure-fluid density ratio (ρ_s/ρ_f) [39]. On the other hand, implicit coupling is robust, computationally expensive and does not introduce stability constraints. Explicit coupling is a good candidate in cases where ρ_s/ρ_f is large, for example air-tissue interaction during phonation of vocal folds in the larynx, while an implicit scheme is needed for low values of ρ_s/ρ_f, for example blood-tissue interaction in cardiovascular flows. In the latter case, the structure will respond strongly even with small perturbations from the fluid and vice versa. In the present paper, $\rho_s/\rho_f \sim 800$ and explicit coupling is used for the simulations.
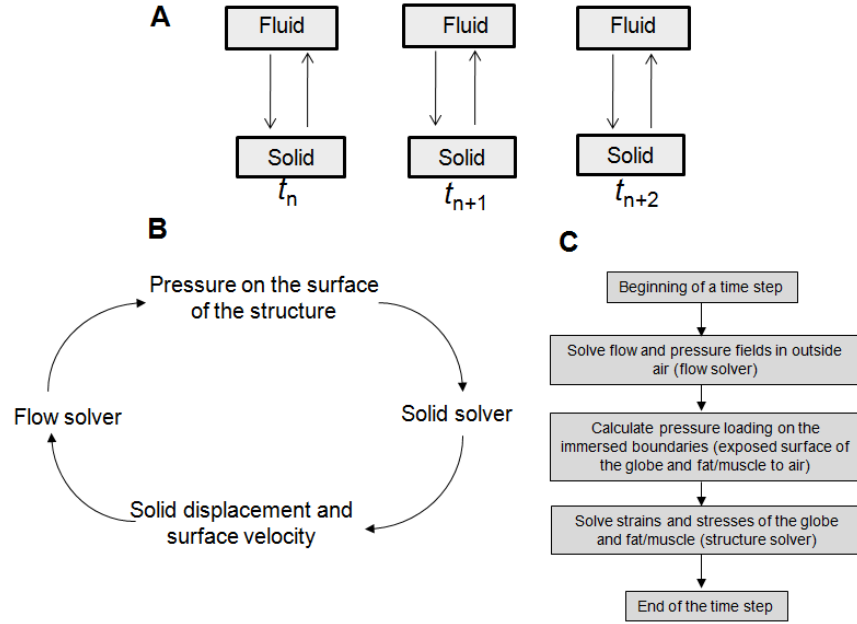

Figure 4: (A) Partitioned approach (B) Data exchange between flow and solid solver (C) Algorithm of FSI solver

In explicit coupling, the flow solution is marched by one time step with the current deformed shape of the structure and the velocities of the fluid-structure interface act as the boundary conditions in the flow solver (Figure 4B). This boundary condition represents continuity of the velocity at the interface (no slip on the solid surface):

$$,\tag{19}$$

The pressure loading on the structure surface exposed to the fluid domain is calculated at the current location on the structure using the interpolated normal fluid pressure at the boundary intercept points via a trilinear interpolation (bilinear interpolation for 2D) as described in Ref. [40]. This boundary condition represents continuity of the traction at the solid-fluid interface:

$$\sigma_{ij,\text{fluid}} n_j = \sigma_{ij,\text{structure}} n_j \; ,\tag{20}$$

9

where n_j is the local surface normal pointing outward from the surface. The structure solver is marched by one time step with the updated fluid dynamic forces (Figure 4C).

2.3.1 Immersed boundary method

The compressible Navier-Stokes equations for the fluid flow with complex structure boundaries inside the fluid domain were solved using the sharp-interface immersed boundary method of Mittal et al. [40]. In this method, the surface of the structure and the fluid domain are represented by an unstructured surface mesh and a Cartesian grid, respectively. The surface mesh of the structure and Cartesian grid of the fluid domain consists of triangular elements and cells (cube or cuboids), respectively. The surface mesh is "immersed" inside the fluid grid. At the pre-processing stage before integrating governing equations, the cells of the fluid domain were marked according to their location with respect to the surface mesh. The cells whose centers were located inside the surface mesh were identified and tagged as "body" cells and the other points outside the surface mesh were "fluid" cells as shown in Figure 5. Note that only cell centers are shown in Figure 5. Any body-cell which has at least one fluid-cell neighbor was tagged as a 'ghost-cell' (Figure 5). The center of this ghost cell is referred to as a "ghost point". The boundary condition on the surface mesh was imposed by specifying an appropriate value at the ghost-point. A "normal probe" was extended from the ghost point to intersect the surface mesh. This intersection point is referred to as the "body intercept". The probe was further extended into the fluid to the "image point" such that the body-intercept lies midway between the image and ghost points. A linear interpolation was used along the normal probe to compute the value at the ghost point based on the boundary-intercept value and the value estimated at the image-point. The value at the image-point itself was computed through a tri-linear interpolation from the surrounding fluid nodes. This procedure leads to a nominally second-order accurate specification of the boundary condition on the surface mesh [40].
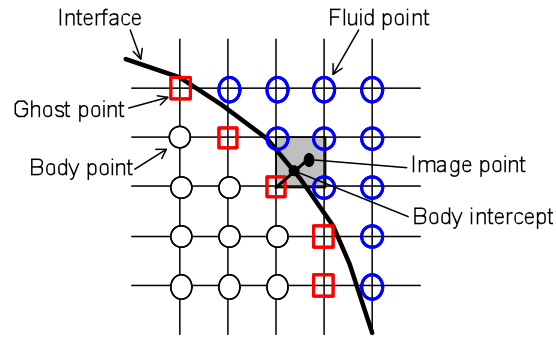

Figure 5: Schematic of the immersed boundary method

2.3.2 Initial conditions associated with the blast

The explosion of TNT produces a mixture of gases in the form of a "fireball" with high temperature and velocities [41]. McNesby et al. [41] measured the shock front velocity and temperature for an unconfined explosion of 2 kg TNT charge. In this experiment, the

shock wave separated from the fireball after 1 ms of the explosion. The radius of the fireball was measured 1.8 m at this instance. We applied the measured velocity and temperature of the shock front from McNesby et al. [41] as an initial condition for the simulations at a radial distance of 1.8 m from the center of the explosion. Figure 6 shows the shock front velocity as a function of the distance for 2 kg TNT. The pressure of the shock-front for unconfined TNT explosions was well-documented by Kingery and Bulmash [42]. This data was later revisited by Swaidak [43] and is available in the form of scaled distance and mass of the TNT. It has been widely accepted by researchers and the fitted curves have been implemented in the ConWep code of ARL and LS-DYNA. We applied the pressure measured for the shock front generated by a 2 kg TNT explosion at 1.8 m from the center of the explosion [42, 43]. The Gaussian profiles of the initial pressure and velocity are shown in Figure 7A and the initial temperature for the shock wave is shown in Figure 7B. The initial condition elsewhere in the computational domain was set to zero for velocity, and ambient value for the pressure and temperature.
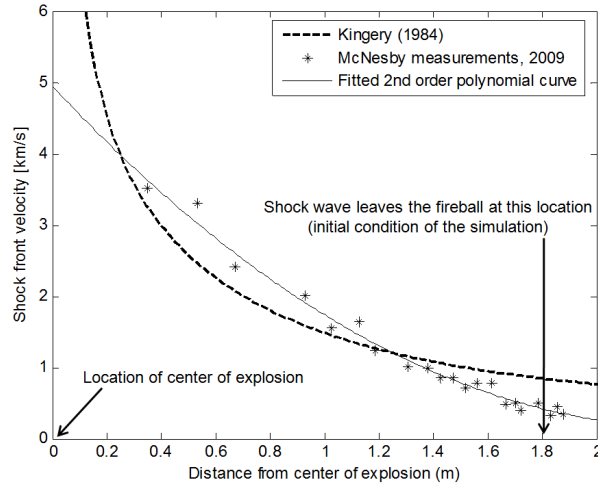

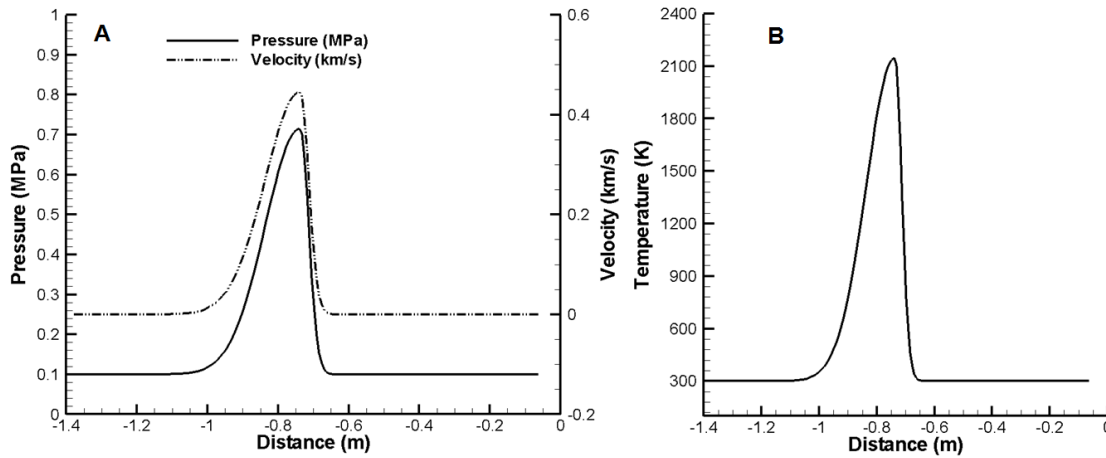Figure 6: Shock front velocity as a function of distance. Points represent measurements by McNesbyet al. [41].

Figure 7: Initial conditions for the pressure, velocity and temperature.

11

3   Results and Discussion

We considered a 2 kg TNT explosion in front of the face at a distance of 2.5 m (Figure 8). These parameters are based on the conditions of field tests for blast exposure, conducted by the US Army Research program [41]. The fluid-structure interaction (FSI) solver presented in the previous section was employed to simulate the propagation of the three-dimensional blast wave. The grid stretching boundary condition was applied on all boundaries of the computational domain shown in Figure 8. This section is organized as follows. First, we present the results of pressure loading using the rigid skin model in Section 3.1. In Section 3.2, we use the skull model to characterize the deformation of the globe caused by blast pressure loading. Next, we present sensitivity study of the computational model to material properties (section 3.2.1) and anatomical parameters (section 3.2.2). Finally, we predict possible eye injuries and associated injury risks using the calculated intra-ocular pressure (IOP) and von-Mises stress in the sclera (section 3.3); and discuss limitations of our model in section 3.4.
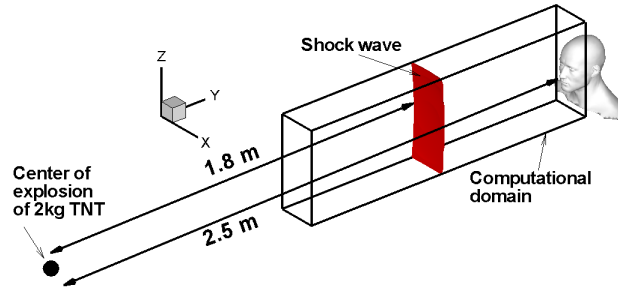

Figure 8: Simulation set up

3.1   Effect of facial features on blast wave reflections around the eye

For these simulations, the skin and all facial features including the eye were treated as rigid structures. The flow fields in the sagittal plane obtained by the fluid-structure interaction simulations are shown in Figure 9A. There were extensive reflections of the blast wave by the nasal and brow ridges. Together, they formed a reflector that focused the incident blast wave on the eye (Figure 9A). This effect allows a planar blast wave with a pressure p just before impacting the face to apply a peak pressure of $4p$ (1.4 MPa) on the eye during the impact. These reflections also produced an asymmetric pressure loading on the eye (Figure 9B) that was higher nearer to the nasal bone than the zygomatic bones. Figure 10 shows the time-variation of the pressure on the numerical probes A, B and C shown in Figure 9B. The peak pressure at probe B was around two times higher than the pressures at probes A or C, which confirms the asymmetric nature of pressure loading. The time-scale in Figure 10 further illustrates the highly transient and asymmetric nature of the pressure loading developed from blast wave interactions. The duration of pressure loading on the face was less than 1 ms (Figure 10), which is 300

times faster than the blink of the eye (~ 300 ms) [44]. Note that the thermal front propagation was slower as compared to the shock wave. The shock wave travelled around 0.7 m in 1 ms to reach the eye while the thermal front propagated only 0.25 m in this time. This can be attributed to the low thermal conductivity of the air.
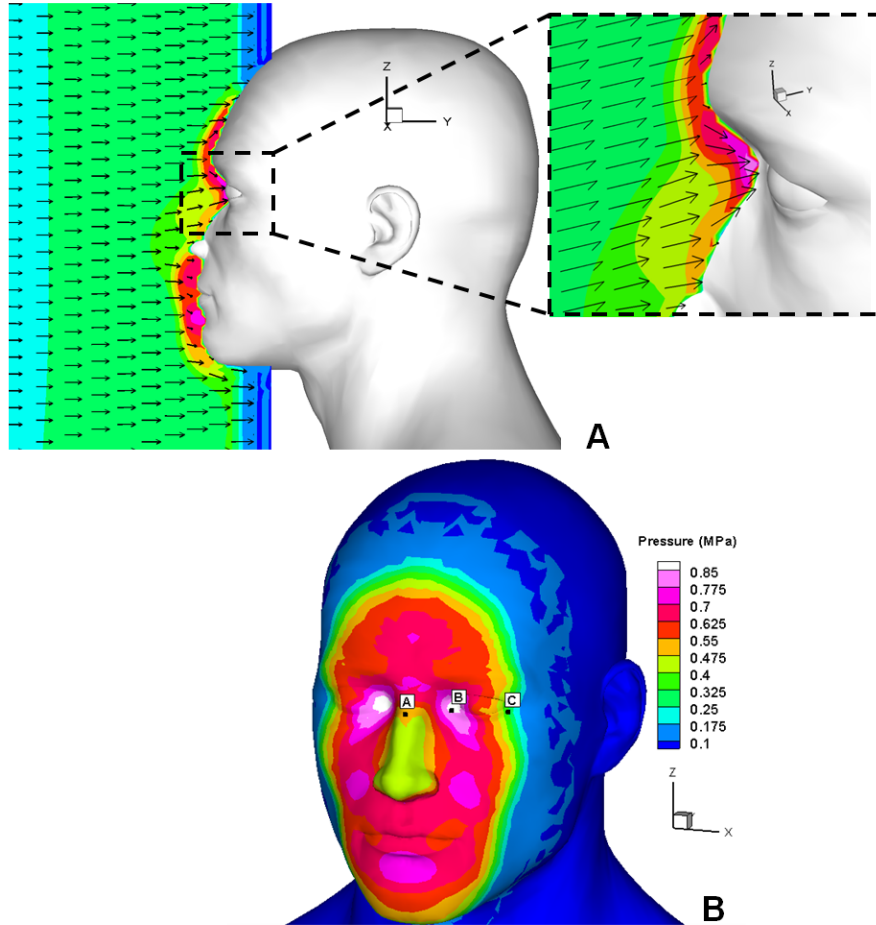

Figure 9: (a) Flow field and pressure contours are shown in sagittal plane. Velocity vectors are shown at every 10th grid point. Zoomed in view of the brow area is shown to illustrate the blast-wave reflections (b) Pressure contours on the face at the instance of the maximum pressure loading during the impact the blast wave. The pressure of the blast front was 0.34 MPa just before the impact.
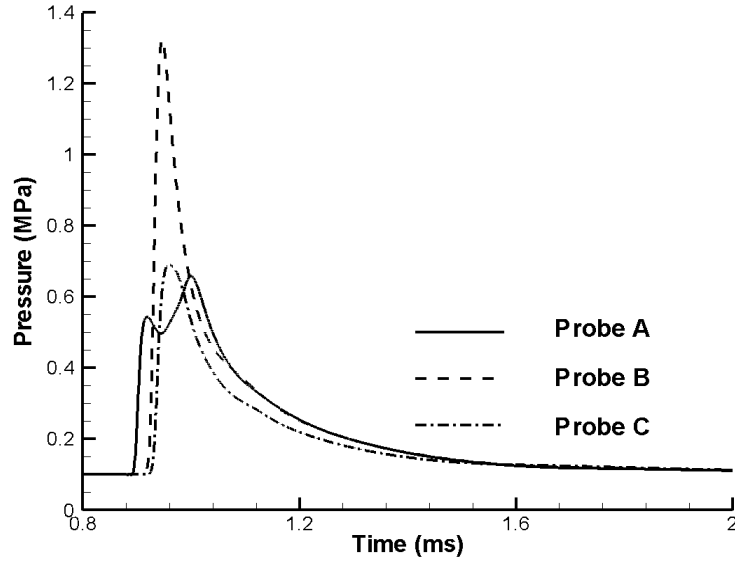
Figure 10: Comparison among time-varying pressures at probes A, B and C shown in the Fig 1B.

3.1.1 Influence of blast location

The influence of the location of the explosion was evaluated for a 2 kg TNT explosion on the ground at a distance of 2.5 m (Figure 11). Simulations of the blast on the ground suggested a similar asymmetric pressure loading on the eye as described in previous section. The peak pressures on probe B shown in Figure 9B are plotted in Figure 12. We note a 40% decrease in peak pressure for the explosion on the ground as compared to that in front of the face. The flow field shown in Figure 13 illustrates that the nasal and brow ridges do not act as an effective reflector of the incident wave in this case.
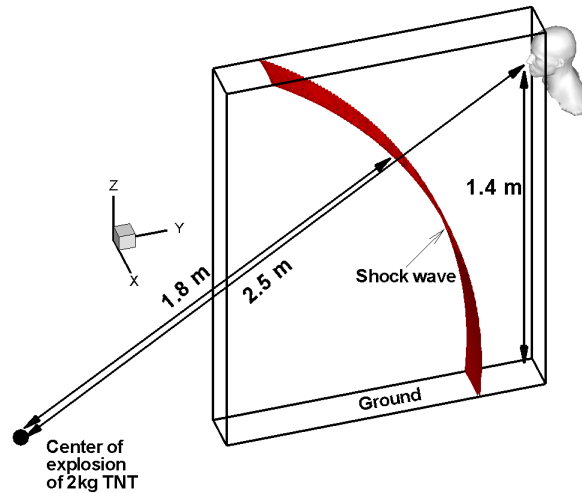

Figure 11: Initial condition of the simulation for investigating influence of blast location.
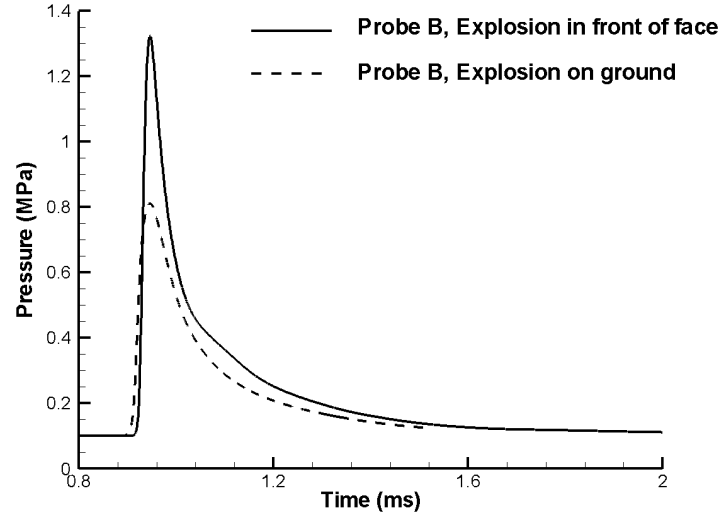
14

Figure 12: Comparison between time-varying pressures at probe B for the explosions in front of face and on the ground.
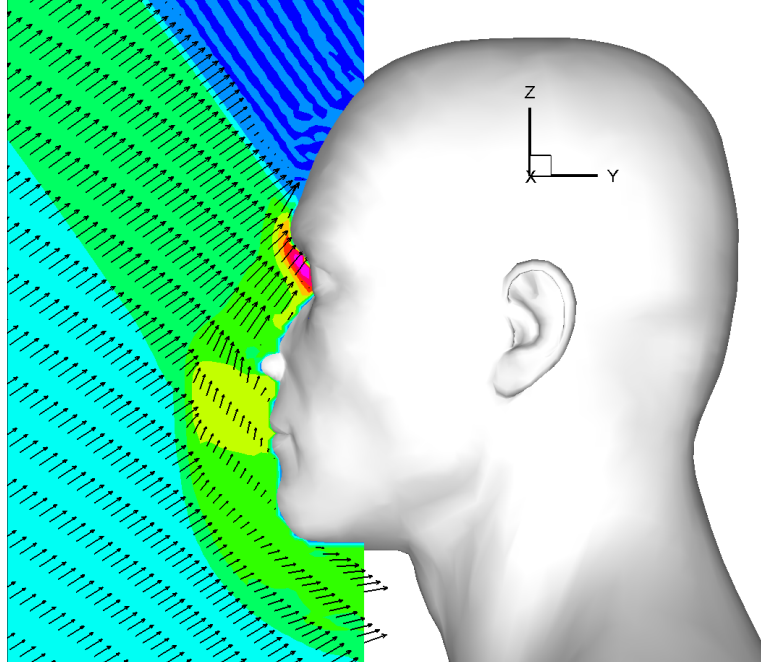

Figure 13: Flow field and pressure contours are shown in sagittal plane. Velocity vectors are shown at every 10th grid point. The pressure levels are same as shown in Figure 9B.

3.2 Biomechanical model of the eye orbit (baseline case)

The skull model described in section 2.2.1 was used to evaluate the deformation response of the eye to the incident blast wave. All deformable solids, namely, internal solid, corneo-scleral shell and outer solid were treated as neo-Hookean quasi-incompressible solids in the structure model (Eq. 14). The calculated peak pressure loading on the skull model was 30% lower as compared to the skin model. The time variation of the pressures on probes A, B and C is shown in Figure 14 and the locations of the probes are shown in the inset of Figure 14. The peak pressure (~ 0.9 MPa) was recorded on probes A and B.

15

In the skull model, removing the skin layer decreased the brow protrusion and the lower cartilaginous part of the brow, which decreased the wave reflections on the eye. Hence, the peak pressure was lowered by 36% as compared to the skin model. The skull model also exhibited asymmetric pressure loading on the eye. We examined the question of whether the pressure loading on the eye changes due to globe deformation, and determined that globe deformation had a negligible effect (less than 1%) on the loading for these cases.
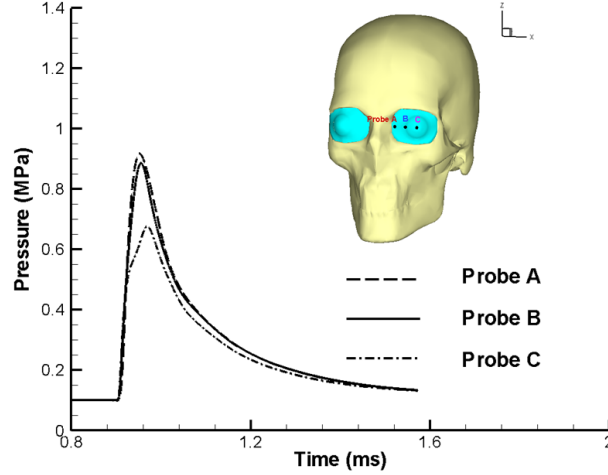

Figure 14: Comparison among time-varying pressures at probes A, B and C shown in the inset.

The time-varying maximum principal stress (s_1) of the corneo-scleral shell and intra-ocular pressure (IOP) are plotted in Figure 15A and s_1 as well as IOP increased overall with time in addition to their periodic behavior. The overall increase was due to the time-varying pressure loading boundary condition and the periodic behavior of the stress and IOP can be explained by the wave propagation inside the orbit as follows. The blast wave travels inside the globe and the outer solid and becomes scattered when contacting the bony wall of the orbit. This induces a periodic behavior of the intra-ocular pressure. To verify this hypothesis, we performed a first-order time scaling analysis of the wave propagation as follows. The time period of the longitudinal wave traveling inside the orbit is given by $T \sim L/v$, where L is the distance of the cornea to the orbital wall (= 36.36 mm) and v is the velocity of the longitudinal wave, given by,

$$v = ((K + 1.3G)/\rho)^{1/2}$$ (16)
,

Where K and G are the bulk and shear moduli, respectively and ρ is the density. We considered $K >> G$ (Table 2) and averaged the values of K and ρ for the inner solid, the corneo-scleral shell and the outer solid to calculate v in the above equation. The time period calculated by the scaling analysis was around 0.03 ms. The time period calculated from the simulation was around 0.07 ms (Figure 15A), which is on the same order of the value calculated by the scaling analysis. We therefore conclude that the periodic behavior of the stress and maximum IOP is due to wave scattering inside the orbit.

The pressure contours in the transverse plane are shown in Figure 15B. The pressure was calculated as the mean of the three components of the principal stress. In Figure 15B, the highest pressure can be noticed near the orbital wall due to the wave

16

scattering by the orbital wall. We note that the pressure is highest in the posterior region inside the inner solid. The grid points (red dots) where the IOP exceeded 0.35 MPa at 1.52 ms are shown in the inset of Figure 15A. The contours of the von Mises stresses in the transverse plane are plotted in Figure 15C, in which the largest von Mises stresses appeared in the sclera near the limbus. Due to asymmetric pressure loading (as explained in section 3.1), the globe distorted relative to the orbital tissue and resulted in significant distortion of the sclera (Figure 15C).
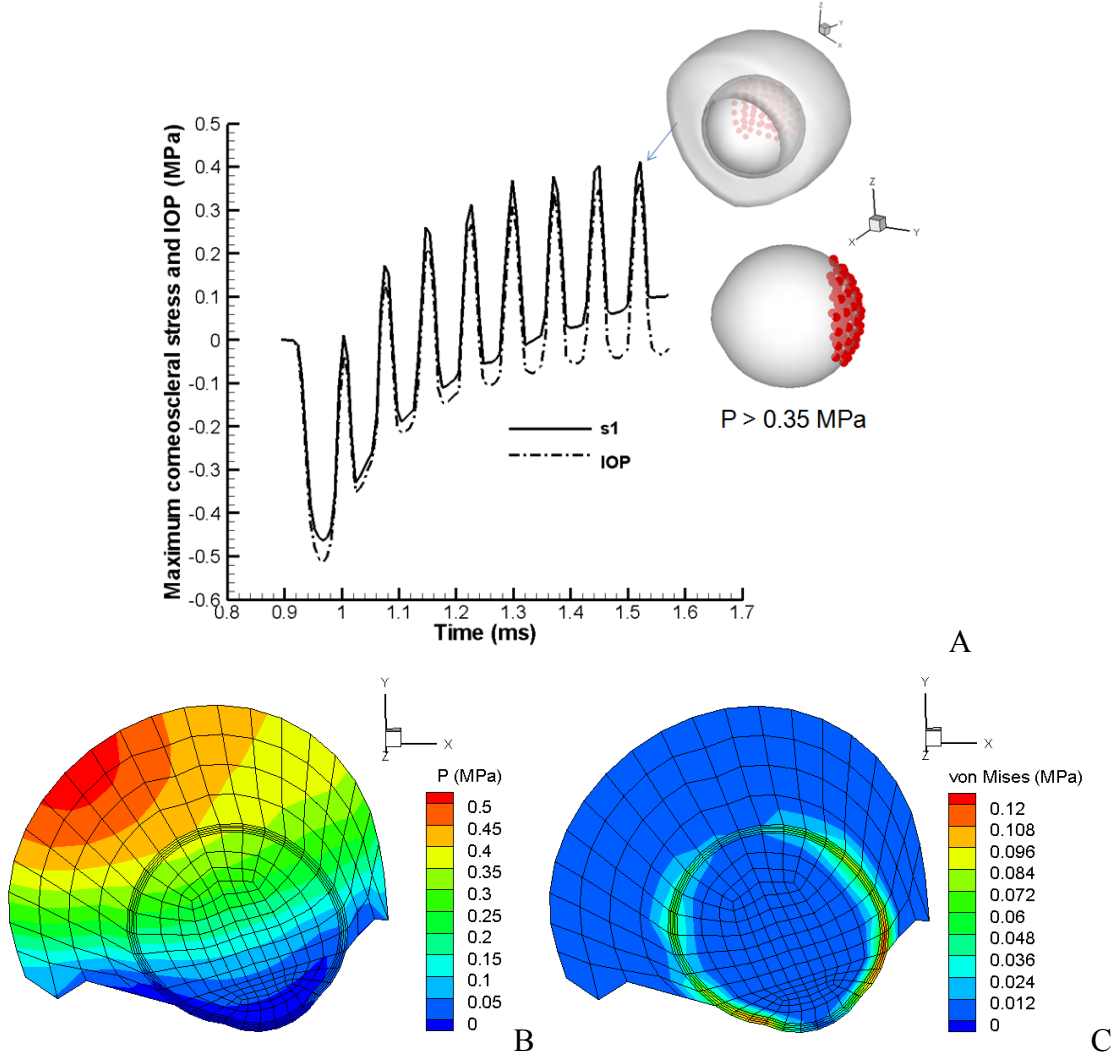

Figure 15: (A) Time-varying corneoscleral principal stress (s_1) and maximum intraocular pressure (IOP) (B) Maximum pressure in the transverse plane of the orbit. Distortion of the globe due to the blast wave is shown by the deformed mesh. (C) von Mises stress shown in the transverse plane, which is the largest in the sclera near limbus.

3.2.1 Sensitivity of the model to material properties

We conducted a sensitivity study of material properties of the corneo-scleral shell and outer solid on the deformation response of the globe. The bulk moduli of the inner solid, corneo-scleral shell, and outer solid were not varied and the values used in the simulation are given in Table 2. The shear moduli of the corneo-scleral shell and outer solid were varied as shown in Table 3. The shear modulus of the outer solid was decreased by 4.4 times in case 1 and increased to a very high value in case 2. Case 2 represents non-deformable extra-ocular tissues and represents a wall boundary condition on thesclera. In case 3, the shear modulus of the outer solid was kept the same as in the baseline case while increasing the shear modulus of the corneo-scleral shell 10-fold, which is on the order of the scleral modulus measured for high pressure rates [33].

Cases	$G_{\text{corneo-scleralshell}}$ (MPa)	$G_{\text{outer solid}}$ (Pa)
Baseline	1	500
Case 1	1	113
Case 2	1	1.4e9
Case 3	10	500

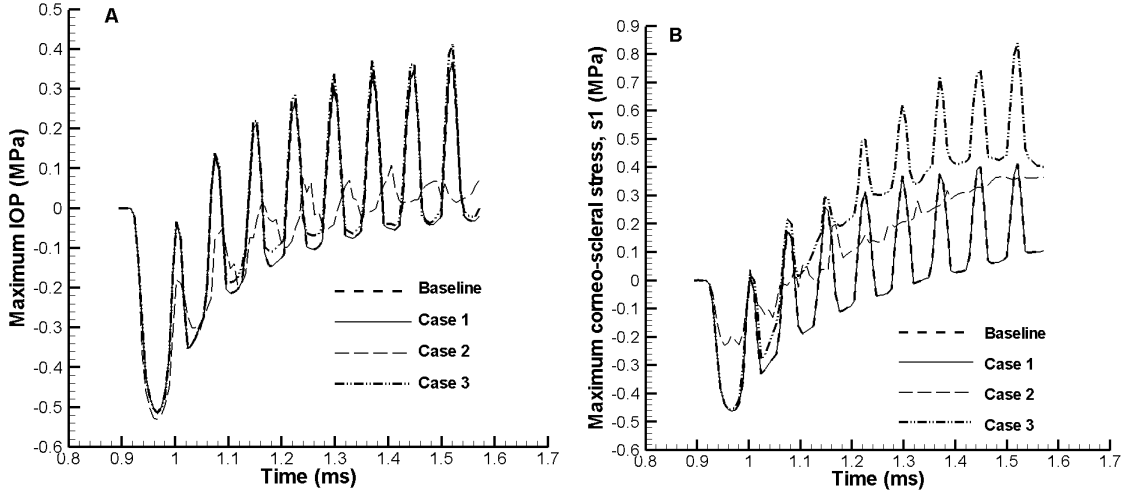Table 3: Simulation cases for sensitivity to material properties.

Figure 16: Comparison among four cases with different material properties for time-varying corneo-scleral principal stress, s_1 (A) and maximum intraocular pressure, IOP (B).

The comparison of time-varying maximum IOP and the corneo-scleral principal stress, s_1 for the four cases described above is shown in Figure 16A and 15B, respectively. The maximum IOP and corneo-scleral stress for the baseline case and case 1were almost the same. It indicates that the decreasing shear modulus of the outer-solid by 4.4 times did not influence the results.

The maximum IOP and corneo-scleral stress shown in the transverse plane for case 2 are shown in Figure 17. We notice that the maximum IOP and corneo-scleral stresses decreased 90% and 10% respectively as compared to the baseline case (Figure

17). This can be attributed to the very high shear modulus of the outer solid which acted as a wall-like boundary condition and reduced the scattering of the travelling wave in the orbit. This reduced the normal deformation of the posterior globe but increased the distortional deformation of the anterior globe. As a result, normal stresses (which occurred mainly in the posterior globe) were smaller but von Mises stresses in the anterior corneal-scleral shell were larger. This also explains why the region of maximum IOP in Fig. 17A shifted from the posterior region (baseline case in Fig 15B) to the anterior region of the globe.

The sensitivity of the shear modulus of the corneo-scleral shell was investigated by increasing it 10 times as in the baseline case and von Mises stresses in the corneo-scleral shell increased by 4 times, as shown in Figure 18.
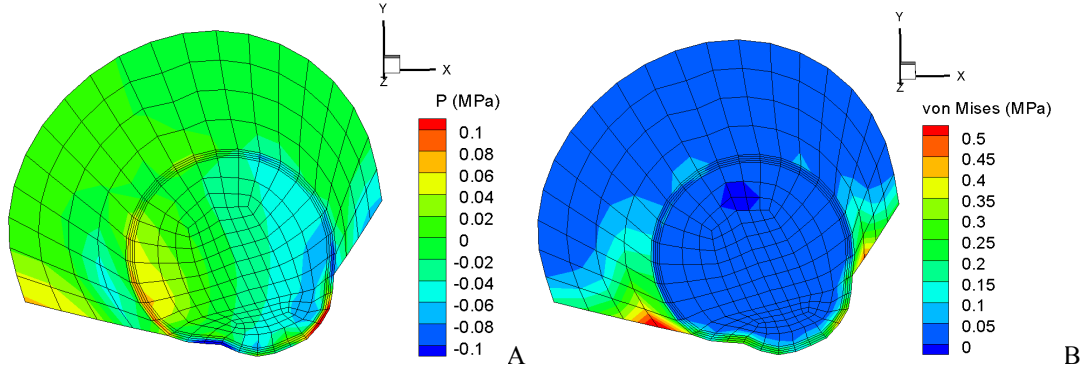

Figure 17: (A) Maximum pressure in the transverse plane of the orbit for case 2. Distortion of the globe due to the blast wave is shown by the deformed mesh. (B) von Mises stresses shown in the transverse plane, which is the largest in the extra-ocular tissue.
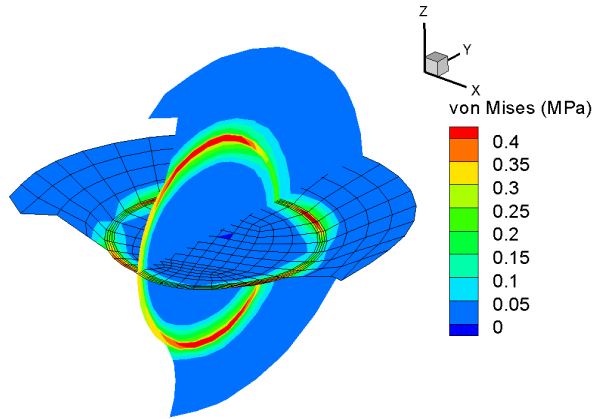

Figure 18: von Mises stresses shown in the transverse and sagittal plane for case 3.

3.2.2 Sensitivity of the model to anatomical parameters

In this section, we present the simulations for understanding the sensitivities to anatomical parameters in the model. The value of LP was increased in case 4, keeping LD same (Table 4). The range of variation of LP was based on the reported anatomical measurements for 39 subjects by Weaver et al.[14].

Cases	LP (mm)	LD (mm)

19

Baseline	12	19
Case 4	18	19

Table 4: Anatomical parameter (LP) variation selected for the sensitivity study.

In Figure 19, we noticed around 50% reduction in the IOP and corneo-scleral stress in case 4 with the increased lateral protrusion (LP). This can be explained by the change in spatial variation of pressure loading on the eye due to change in anatomy of the eye. A comparison of the pressure field in the transverse plane for the two cases is shown in Table 4. The pressure loading was more concentrated on the extra-ocular tissues in case 4 as compared to the baseline case. The reflections from the protruded eye with higher lateral protrusion (LP) altered the spatial gradient of pressure on the eye as shown in Figure 20.
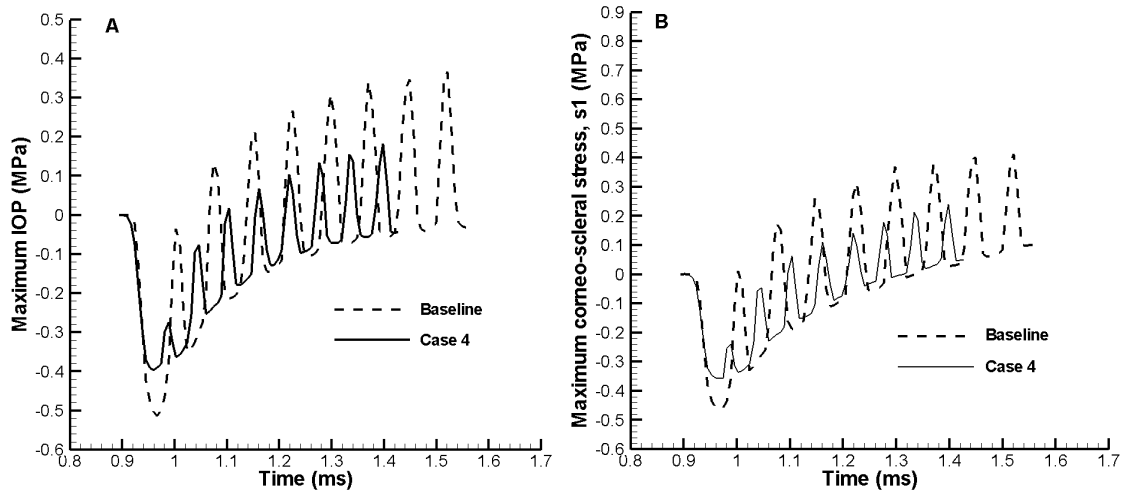

Figure 19: Comparison of time-varying corneo-scleral principal stress (A) and maximum intraocular pressure IOP (B) betweentwo cases with different lateral protrusion (LP).
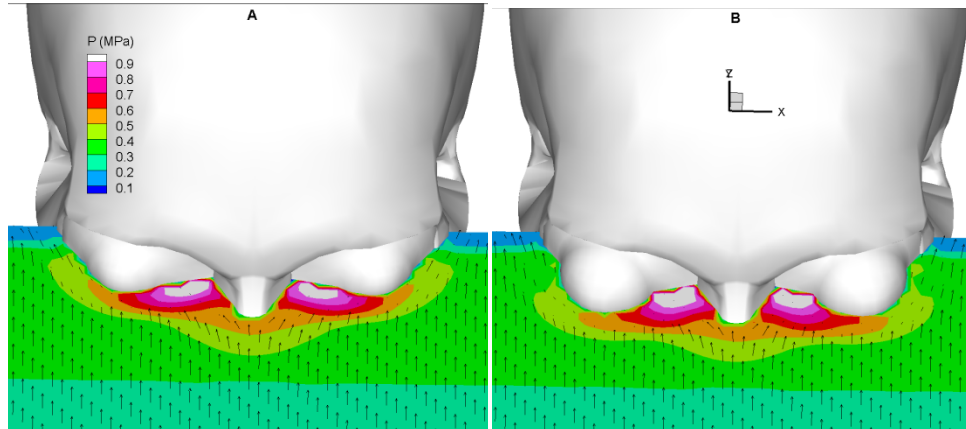

Figure 20: Comparison of pressure field outside the eye between two cases with different anatomical parameter (A) Baseline, LP = 12 mm (B) Case 4, LP 18 mm.

20

3.3 Implications to the eye injury

As shown in Figure 15A for the baseline case, the maximum IOP inside the globe reached 0.42 MPa, corresponding to around 3000 mm Hg, which is two orders of magnitude larger than the 15 mm Hg physiologic IOP for a healthy eye. The von Mises stresses were calculated largest in the sclera wall at the site of muscle attachments, which indicates significant muscle tearing or rupture inside the eye. We assessed the risk of eye injury using the functions published by Duma and Kennedy [45]. These injury risk functions were reported using measurements for blunt impact on the eye by a projectile and can be expressed as [45]:

$$Injury\_risk = \left[\frac{1}{1 + e^{a-bx}} \right] 100\%,$$

where x is projectile normalized energy [kJ/m^2], a is a dimensionless parameter that depends on the injury type and parameter b is expressed in terms of m^2/kJ. The values of a and b for different injury types were reported in Ref. [45]. Recently, Alphonse et al. [46] calculated the injury risk for an increased IOP using correlation between the projectile normalized energy and the IOP by Duma et al. [47]. The calculated percentage of injury risks corresponding to the maximum IOP value 0.42 MPa for our simulation are around 98%, 14%, 0%, 0%, 0.02% respectively, for corneal abrasion, hyphema, lens dislocation, retinal damage and globe rupture. We summarize recent relevant clinical and experimental studies of primary ocular blast injury to provide context for our numerical data and injury risk analysis. Cockerham et al. [48] studied combat veteran in-patients (n = 46) with documented blast-induced traumatic brain injury in Iraq and Afghanistan. The closed-eye injuries such as corneal abrasion, vitreous haemorrhage, retinal detachment and optic nerve atrophy were found in 43% of the patients and it was noticed that patients outside the military vehicles had higher levels of ocular injury than did those situated within military vehicles [48]. These authors attributed this to closer proximity to the blast source, with attendant high blast overpressure, and the protective effect of armoured vehicles against blast waves and fragmentation. Hines-Beard et al. [49] reported primary ocular blast injury on mice, which were exposed to a maximum of 0.21 MPa blast pressure. In these experiments, increased ocular damage was reported with increased blast pressures and the following closed eye injuries were reported: corneal edema, corneal abrasions, and optic nerve avulsion.

3.4 Limitations of the computational model

The present work contains a number of limitations. The model for the eye-wall assumed a uniform thickness, though the thickness of the human cornea varies from 0.5-0.8 mm from apex to limbus [50] and the thickness of the sclera can vary from 0.3-1.2 mm. The sclera is thickest at the limbus and posterior region and thinnest at the equator and peripapillary region. The tissues of the cornea and sclera were assumed to be isotropic and spatially homogeneous, but X-ray diffraction experiments have demonstrated significant anisotropy in the limbus [51] and peripapillary regions of the sclera [52]. The neo-Hookean model furthermore could not capture the dramatic strain stiffening stress response for pressures. We are currently working on incorporating more detailed description of the spatially varying thickness and collagen-derived anisotropy of the

cornea and sclera in the computational model to investigate their effects on the deformation and stress response of the globe to blast. The computational model also does not include important intraocular components such as the lens, retina, and optic nerve head. These components will be included in future models to investigate the risk for such injuries as lens dislocation, retinal detachment, and optic nerve avulsion. We will apply the more detailed computational model to investigate the ability of current eye protective equipment to reduce the effects of blast loading on the globe.

4 Summary

A fluid-structure interaction computational model was presented for blast wave impact on the human eye. We simulated the propagation of the blast wave in three-dimensional coordinates to obtain the transient flow-fields and pressure loading on the human eye. The reflections of the blast wave from the nasal and brow ridges amplify the pressure loading and produce asymmetric loading on the eye. We predicted possible eye injuries and associated injury risks using the calculated intra-ocular pressure (IOP) and von-Mises stress in the sclera. The sensitivity study of the model to material properties and anatomical parameters was presented and discussed. The highest injury risk from blast loading was associated with cornea abrasions and the low IOP experienced by the globe were too low to produce an appreciable risk for globe rupture. The maximum IOP was found at the posterior sclera, which may increase the risk for delayed injuries to the optic nerve head. The high distortional deformation at the muscle attachment site may also cause appreciable risk for muscle tearing and globe dislocation.

5 Acknowledgements

6 References

[1]Ari AB. Eye injuries on the battlefields of Iraq and Afghanistan: public health implications. Optometry 2006;77:329-339.

[2]Belkin M, Treister G, Dotan S. Eye injuries and ocular protection in the Lebanon War, 1982. Isr J Med Sci 1984;20:333-338.

[3]Weichel ED, Colyer MH, Ludlow SE, Bower KS, Eiseman AS. Combat ocular trauma visual outcomes during operations Iraqi and Enduring Freedom. Ophthalmology 2008;115:2235-2245.

[4]Mader TH, Carroll RD, Clifton SS, George RK, Ritchey P, Neville P. Ocular war injuries of the Iraqi Insurgency, January-September 2004. Ophthalmolog 2006;113:97-104.

[5] Medical Research for Prevention, Mitigation, and Treatment of Blast Injuries.Department of Defense Directive Number 6025.21E. July 5, 2006. http://www.dtic.mil/whs/directives/corres/pdf/602521p.pdf

[6] Abbotts R, Harrison SE, Cooper GL. Primary blast injuries to the eye: a review of the evidence. *JR Army Med Corps 2007;153:119-123.*

[7] Duke-Elder S. Concussion injuries. Text-book of Ophthalmology, Vol VI: Injuries. London: Henry Kimpton; 1954; 5751-961.

[8] R Scott. (2011). The injured Eye, Phil. Trans. Roy. Soc. B Vol 366 p 251

[9] Hamit, H. F. 1973 Primary blast injuries. Ind. Med. 3, 142.

[10] Wharton-Young, M. 1945 Mechanics of blast injuries.War Med. 8, 2.

[11] Uchio E, Ohno S, Kudoh J, Aoki K, Kisielewicz LT. Simulation model of an eyeball based on finite element analysis on a supercomputer. Br. J. Ophthalmol. 1999;83:1106-1111.

[12] Stitzel J, Duma S, Herring I, Cormier J. (2002) "A Nonlinear Finite Element Model of the Eye with Experimental Validation for the Prediction of Globe Rupture," Stapp Car Crash Journal, Vol. 46, pp. 81-102

[13] AA Weaver, EA Kennedy, SM Duma, JD Stitzel (2011) "Evaluation of Different Projectiles in Matched Experimental Eye Impact Simulations ," J BiomechEngg. Vol 133, p 31002.

[14] AA Weaver, KL Loftis, SM Duma, JD Stitzel (2011) "Biomechanical modeling of eye trauma for different orbit anthropometries," J Biomechanics.Vol 44, p 1296.

[15] J Al-Sukhun, Christian Lindqvist and RistoKontio (2006) Modelling of orbital deformation using finite-element analysis J R SocInterface. Vol 3(7) p 255-62.

[16] J Al-Sukhun, R Kontio and C Lindqvist and Risto (2006)Orbital Stress Analysis—Part I: Simulation of Orbital Deformation Following Blunt Injury by Finite Element Analysis Method J Oral Maxillofac Surg. Vol 64(3) p 434-42.

[17] S Cirovic, R M Bhola, D R Hose, I C Howard, P V Lawford, J E Marr, M A Parsons. (2006) Computer modelling study of the mechanism of optic nerve injury in blunt trauma.Br J OphthalmolVol 90 p 778–783.

[18] S.Lele. (1992). Compact finite Difference Schemes with Spectral-like Resolution, J Comp. Phys. Vol 103, p 16.

[19] Gaitonde, D., Shang, J. S., and Young, J. L., (1999) Practical Aspects of Higher-order Accurate Finite Volume Schemes for Wave Propagation Phenomena, *International Journal for Numerical Methods in Engineering*, Vol. 45, 1999, pp. 1849-1869

[20] Kawai, S. and Lele, S. K., (2008) Localized Artificial DiffusivityScheme for Discontinuity Capturing on Curvilinear meshes," *J. Compt. Phys.* 227, 22.

[21] Cook, A. W. and Cabot, W. H., (2005) Hyper Viscosity forShock-turbulence Interactions, *J. Compt. Phys.* 203,2, pp.379-385.

[22] Holzapfel GA (2006). Nonlinear solid mechanics.John Wiley and Sons, New York.

[23] Tahoe is an open source C++ finite element solver, which was developed at Sandia National Labs, CA (http://sourceforge.net/projects/tahoe/).

[24]Hughes T. J. R. (1987).The Finite Element method. Prentice-Hall. Englewood Cliffs, NJ, Chapter 9.

[25]Zygote Media Group, Inc is a developer company for computer-generated 3D graphical software, and of late has specialized in the enhanced visualization of the human anatomy (http://www.zygote.com/).

[26]Altair HyperMesh is a high-performance finite element pre-processor that provides an interactive environment for mesh development and analysis (http://www.altairhyperworks.com/).

[27] AA Weaver, KL Loftis, JC Tan, SM Duma, JD Stitzel (2010) "CT based three-dimensional measurement of orbit and eye anthropometry," Invest Ophthalmol Vis Sci. Vol 51(10), p 4892-7.

[28]CUBIT is a geometry and mesh generation toolkit developed at Sandia National Laboratories (http://cubit.sandia.gov/).

[29]Schutte S, van den Bedem SPW, van Keulen F, van der Helm FCT, Simonsz HJ. (2006) Finite-element analysis model of orbital biomechanics. Vision Res. Vol 46, p 1724.

[30]Duck FA (1990). Physical Properties of Tissue: A Comprehensive Reference Book. London.. Academic press, p 77-78, 138

[31]Nickerson CL, Park J, Kornfield JA, Karageozian H. (2008). Rheological properties of the vitreous and the role of hyaluronic acid. J. Biomechanics. Vol 41 p 1840

[32]Bereiter-Hahn J. Advances in acoustic microscopy. Berlin, Germany: Springer; 1995. Probing biological cells and tissues with acoustic microscopy.

[33]Bisplinghoff JA, C McNally, SJ Manoogian and SM Duma. (2009).Dynamic material properties of the human scleraJ. Biomechanics. Vol 42 p 1493.

[34]Computer modelling study of the mechanism of optic nerve injury in blunt trauma, S Cirovic, R M Bhola, D R Hose, I C Howard, P V Lawford, J E Marr, M A Parsons, Br J Ophthalmol 2006;90:778–783

[35]Power, E. D. 2001 A nonlinear finite-element model of the human eye to investigate Ocular injuries from night vision goggles. M.S. thesis, Virginia Polytechnic Institute and State University, Virginia.

[36]Modelling of orbital deformation using finite-element analysis Jehad Al-Sukhun, Christian Lindqvist and RistoKontio, J. R. Soc. Interface (2006) 3, 255–262

[37]Schoemaker I, Hoefnagel PPW, Mastenbroek TJ, et al. Elasticity viscosity and deformation of the retrobulbar fat in eye rotation. Invest Ophthalmol Vis Sci 2004;45(suppl 2):U651

[38]Bhardwaj R. and Mittal R. (2012). Benchmarking a Coupled Immersed-Boundary-Finite-Element Solver for Large-Scale Flow-Induced Deformation, AIAA Journal. *AIAA Journal.* Vol 50 (7), pp. 1638-1642.

[39]Zheng X., Xue Q., Mittal R. and Beilamowicz S. (2010). A Coupled Sharp-Interface Immersed Boundary-Finite-Element Method for Flow-Structure Interaction with Application to Human Phonation", *Journal of Biomechanical Engineering*. Vol. 132, 111003 (1-12).

[40]Mittal, R., Dong, H, Bozkurttas, M., Najjar, F.M., Vargas, A. and vonLoebbeck, A. (2008). A Versatile Immersed Boundary Methods for Incompressible Flows with Complex Boundaries.*J. Comp. Phys*. Vol.2 27 (10).

[41]KL McNesby, BE Homan, JJ Ritter, Z Quine, RZ Ehlers, BA McAndrew (2010). After burn Ignition Delay and Shock Augmentation in Fuel Rich Solid Explosives. *Propellants, Explosives andPyrotechnics*, Vol 35, pp 57 – 65

[42]CN Kingery, G Bulmash (1984).Airblast Parameters from TNT Spherical Air Burst and Hemispherical Surface Burst, Defence, Tech. Rep. Report ARBL-TR-02555, U.S. Army BRL, Aberdeen Proving Ground, MD.

[43]Swisdak, M.: Simplified kingery airblast calculations. In: Minutes of the 26th DOD Explosives Safety Seminar (1994). Available at http://www.dtic.mil/cgi-bin/GetTRDoc?AD=ADA526744

[44]Tsubota K, Hata S, Okusawa Y, Egami F; Ohtsuki T; Nakamori K, Quantitative Videographic Analysis of Blinking in Normal Subjects and Patients With Dry Eye, *Arch Ophthalmol*. 1996; Vol 114(6):715-720.

[45]Kennedy E and Duma S (2011). Final report: Eye Injury Risk Functions for Human and FOCUS Eyes: Hyphema, Lens Dislocation, and Retinal Damage, Technical report, U.S. Army Medical Research and Material Command Fort Detrick, Maryland. Available at http://www.facstaff.bucknell.edu/eak012/Reports_n_Papers/Eye_Injury_Risk_Functions_for_Human_and_FOCUS_Eyes--FinalReport_W81XWH-05-2-0055--July2011Update.pdf(Accessed July 23, 2012).

[46]Alphonse VD, Kemper AR, Strom BT,Beeman SM, Duma SM, (2012). Mechanisms of Eye Injuries From Fireworks, *JAMA*.Vol 308(1) p 33-34.

[47]Stefan M. Duma, Jill A. Bisplinghoff, Danielle M. Senge, Craig McNally, and Vanessa D. Alphonse, (2012) Evaluating the Risk of Eye Injuries: Intraocular Pressure During High Speed Projectile Impacts, *Current Eye Research,* Vol 37(1), 43–49, 2012.

[48]Cockerham, C.G., Rice, T.A., Hewes, E.H., Cockerham, K.P., Lemke, S., Wang, G., Lin, R.C., Glynn-Milley, C., 2011. Closed-eye ocular injuries in the Iraq and Afghanistan wars. New Engl. J. Med. 364, 2172-2173

[49]Hines-Beard J, Marchetta J, Gordon S, Chaum E, Geisert EE, Rex TS. A mouse model of ocular blast injury that induces closed globe anterior and posterior pole damage. Exp Eye Res. 2012 Jun;99(1):63-70. Epub 2012 Apr 7. PubMed PMID: 22504073.

[50]Kaufman PL, Alm A Adler's Physiology of the Eye, 10 e, Mosby, 2002

[51]Aghamohammadzadeh H, Newton RH, Meek KM. X-ray scattering used to map the preferred collagen orientation in the human cornea and limbus. Structure. 2004 Feb;12(2):249-56.

[52]Pijanka JK, Coudrillier B, Ziegler K, Sorensen T, Meek KM, Nguyen TD, Quigley HA, Boote C. Quantitative Mapping of Collagen Fiber Orientation in Non-glaucoma and Glaucoma Posterior Human Sclerae. Invest Ophthalmol Vis Sci. 2012 Aug 7;53(9):5258-70. 2012.

---

[1]Ari
[2]Belkin
[3]Weichal
[4]Mader
[5]DOD
[6]Abotts
[7]Duke
[8] Scott
[9] Hamit
[10] Wharton

[11]Uchio
[12] Stizel_2002
[13]Weaver_JBE
[14]Weaver_JBM_model
[15]Al-Sukhun1
[16]Al-Sukhun2
[17]Cirovic
[18]lele
[19]Gaitonde
[20]kawai
[21]Cook
[22]Holzapfel
[23]Tahoe
[24]Hughes1987
[25]Zygote
[26]Altair
[27]Weaver_CT
[28]Cubit
[29]Schuttle
[30] Duck
[31]Nickerson
[32]Bereiter
[33]Bisplinghoff
[34]Cirovic
[35] Power
[36] Al-Sukhum
[37]Schoemaker
[38]Bhardwaj
[39]Zheng, 2010
[40]Mittal,2008
[41]McNesby
[42]Kingerybulmash
[43]Swisdak
[44]Tsubota
[45]Keneddy
[46]Duma_JAMA
[47]Duma_riskfunc
[48]Cockerham
[49]Rex
[50]Alder
[51]Aghamohammadzadeh
[52]Pijankal